Author for correspondence:
Alan E. Lindsay
e-mail: a.lindsay@nd.edu

Short-time diffusive fluxes over membrane receptors yields the direction of a signalling source

Alan E. Lindsay[1], Andrew J. Bernoff[2] and Adrián Navarro Hernández[1]

[1]Department of Applied and Computational Math and Statistics, University of Notre Dame, Notre Dame, IN 46617, USA
[2]Department of Mathematics, Harvey Mudd College, Claremont, CA 91711, USA

(iD) AEL, 0000-0001-8221-8668

An essential ability of many cell types is to detect stimuli in the form of shallow chemical gradients. Such cues may indicate the direction that new growth should occur, or the location of a mate. Amplification of these faint signals is due to intra-cellular mechanisms, while the cue itself is generated by the noisy arrival of signalling molecules to surface bound membrane receptors. We employ a new hybrid numerical-asymptotic technique coupling matched asymptotic analysis and numerical inverse Laplace transform to rapidly and accurately solve the parabolic exterior problem describing the dynamic diffusive fluxes to receptors. We observe that equilibration occurs on long timescales, potentially limiting the usefulness of steady-state quantities for localization at practical biological timescales. We demonstrate that directional information is encoded primarily in early arrivals to the receptors, while equilibrium quantities inform on source distance. We develop a new homogenization result showing that complex receptor configurations can be replaced by a uniform effective condition. In the extreme scenario where the cell adopts the angular direction of the first impact, we show this estimate to be surprisingly accurate.

1. Introduction

In a variety of cell types, the ability to locate external stimuli is essential to normal function. Some important examples include eukaryotic gradient-directed cell migration (chemotaxis) [1–3], directional growth (chemotropism) in neurons [4], yeast [5,6] and airinemes in zebrafish [7]. A unifying feature of these systems is that they must infer the spatial location of the
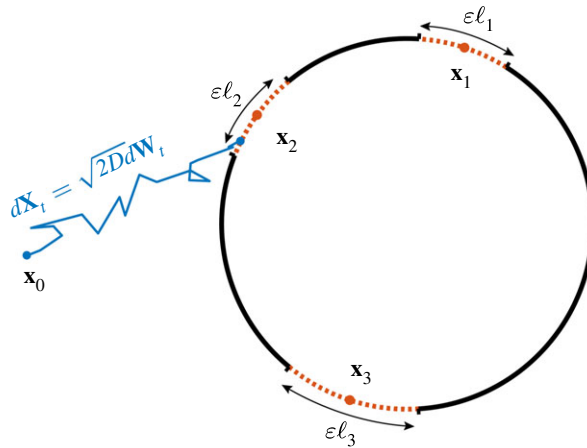
Figure 1. Planar diffusion from a source $\mathbf{x}_0$ to receptors arranged on a disc representing a cell. The non-overlapping receptors have centres $\{\mathbf{x}_k\}_{k=1}^N$ and spatial extent $\{\varepsilon\ell_k\}_{k=1}^N$. Source inference is the task of recovering $\mathbf{x}_0 \in \mathbb{R}^2 \backslash \Omega$ from the statistics of particles incident to the receptors.

external source through the noisy arrivals of diffusing particles to membrane receptors. Many authors have sought to understand how complex downstream machinery, activated by noisy receptor input, enables cells to accomplish this feat of triangulation so robustly [8–16]. In the present work, we focus on the most upstream component of this mechanism, the dynamics of the signal to the receptors.

Signalling molecules undergoing planar diffusive transport will eventually arrive at a receptor (cf. figure 1) and the distribution of arrivals across the set of receptors, known as the *splitting probabilities* [17], encodes information on the source location. In the scenario of planar diffusion, or three-dimensional diffusion to a spherical cell with surface receptors, Dobramysl & Holcman [18,19] demonstrated that a unique source location can be inferred from the splitting probabilities, provided the number of receptors is at least $N = 3$. Biological receptor numbers vary considerably between systems with examples including $N \approx 10^4$ in budding yeast [5] and $N \approx 10^4$–10^5 in lymphocytes [20]. In [21], a maximum-likelihood estimation (MLE) method was developed which enables robust source inference from splitting probabilities for large receptor numbers N. Interestingly, clustered receptor configurations can exhibit improved source inference over homogeneous arrangements.

While these works indicate plausible approaches to infer the direction and possibly the distance of signalling sources, mechanisms for their implementation at a cellular level are challenging to account for due to several factors. First, both the splitting probabilities and the derived MLE are global quantities—their use in source detection implies that a cell has knowledge of its geometry, the spatial configuration of its receptors, together with an ability to store and integrate signals. Second, as we shall demonstrate, the two-dimensional splitting probabilities in the small receptor limit are all equal and independent of the source location. Finally, in the scenario of an unbounded domain, the mean arrival time for an individual signalling molecule to arrive at a receptor is infinite [22], suggesting equilibration to the splitting probabilities may occur on a long timescale. The timescale of this equilibration may or may not be matched by those observed biologically. We note that in contrast to the bounded domain scenario, the timescale for equilibration in the unbounded domain case does not reduce to evaluation of the principal eigenvalue [23]. Furthermore, an equilibrium state may not be applicable if the source location is mobile or its signal dynamic in nature [6,24–26].

In this paper, we suggest that much more information can be gleaned by considering the dynamic problem and that source directionality is most easily inferred from short-time receptor arrivals.

The mathematical formulation for the splitting probabilities draws from the conceptual framework of Berg & Purcell [27]. For a cell represented by $\Omega \subset \mathbb{R}^2$, the splitting probabilities $\{\phi_k(\mathbf{x})\}_{k=1}^N$ encode the likelihood that a particle originating at $\mathbf{x} \in \mathbb{R}^2 \backslash \Omega$ reaches the kth receptor $\partial\Omega_k$ before any others. This satisfies the exterior Laplace mixed boundary value problem

$$\Delta\phi_k = 0, \quad \mathbf{x} \in \mathbb{R}^2 \backslash \Omega; \quad \phi_k \text{ bounded as } |\mathbf{x}| \to \infty \tag{1.1a}$$

and

$$\phi_k = \delta_{jk}, \quad \mathbf{x} \in \partial\Omega_j, \ j = 1, \ldots, N; \ \nabla\phi_k \cdot \mathbf{n} = 0, \ \mathbf{x} \in \partial\Omega_r. \tag{1.1b}$$

We define $\partial\Omega_a := \cup_{j=1}^N \partial\Omega_j$ as the portion of $\partial\Omega$ covered in receptors and $\partial\Omega_r := \partial\Omega \backslash \partial\Omega_a$ as the remaining portion. Here, δ_{jk} is the Kronecker delta function. As discussed above, we consider the dynamic receptor signal described through the probability density $p = p(\mathbf{x}, t)$ satisfying

$$\frac{\partial p}{\partial t} = D\Delta p, \quad \mathbf{x} \in \mathbb{R}^2 \backslash \Omega, \ t > 0; \ p = \delta(\mathbf{x} - \mathbf{x}_0), \ \mathbf{x} \in \mathbb{R}^2 \backslash \Omega, \ t = 0; \quad (1.2a)$$

and

$$p = 0, \quad \mathbf{x} \in \partial\Omega_a, \ t > 0; \ D\nabla p \cdot \mathbf{n} = 0, \ \mathbf{x} \in \partial\Omega_r, \ t > 0. \quad (1.2b)$$

Here, $D > 0$ is the diffusivity of the signalling molecule. For the purposes of inferring source location, the quantities most relevant are the individual receptor fluxes $\{\mathcal{J}_k\}_{k=1}^N$ and the combined receptor flux for the cell, $\rho(t)$, satisfying

$$\mathcal{J}_k(t) = -D\int_{\partial\Omega_k} \nabla p \cdot \mathbf{n} \, dS \quad \text{and} \quad \rho(t) := -D\int_{\partial\Omega_a} \nabla p \cdot \mathbf{n} \, dS = \sum_{k=1}^N \mathcal{J}_k(t). \quad (1.3)$$

The models (1.1) and (1.2) are well-studied conceptual models of receptor activation [13,27–30]. Extensions to this canonical system have studied to account for more intricate biological features such as receptor binding dynamics [31], receptor diffusion [32] and receptor gating [33,34].

In the present work, we develop solutions to (1.1) and (1.2) by means of matched asymptotic expansions in the limit of vanishing receptor size. For the dynamic problem (1.2), we obtain fluxes by first applying a Laplace transform, solving the modified Helmholtz transform equation by matched asymptotic methods, and finally applying numerical inverse Laplace transform. Throughout the analysis of the static and dynamic problems, we adopt the notation that the N receptors are centred at $\{\mathbf{x}_k\}_{k=1}^N$ and occupy a segment of the boundary with arclength $\{\varepsilon\ell_k\}_{k=1}^N$. The receptors are assumed to be well separated from each other and the source $\mathbf{x}_0$, specifically $|\mathbf{x}_j - \mathbf{x}_k| = \mathcal{O}(1)$ as $\varepsilon \to 0$ for $j \neq k$ and $0 \leq j, \ k \leq N$. Our analysis is valid for general cellular geometries Ω in terms of certain Green's functions (discussed below); however, our exposition will focus on a circular cell of radius $r_{\text{cell}} = 1$ with a source at distance $|\mathbf{x}_0| = r_{\text{source}}$ (cf. figure 1). The applicability of this work to a half plane scenario, which has previously been studied in source localization [18], is demonstrated in appendix D. To corroborate results from the hybrid numerical-asymptotic approach, we employ a recently developed kinetic Monte Carlo (KMC) method, which can rapidly and accurately sample all relevant arrival statistics [35].

To perform inference on the source location, we develop in §3 a MLE that connects the receptor arrival counts $\{c_k\}_{k=1}^N$ to the cumulative fractional fluxes $q_k(\mathbf{x}; t)$ through each receptor. This approach leads to the optimization problem

$$\widehat{\mathbf{x}}_{\text{MLE}}(t) = \arg\max_{\mathbf{x}} \mathcal{L}(\mathbf{x}; t), \quad \mathcal{L}(\mathbf{x}; t) = -\sum_{k=1}^N c_k \log[q_k(\mathbf{x}; t)], \quad q_k(\mathbf{x}; t) = \frac{\int_0^t \mathcal{J}_k(\tau) \, d\tau}{\int_0^t \rho(\tau) \, d\tau}. \quad (1.4)$$

The cumulative fractional fluxes have limiting behaviour $\phi_k(\mathbf{x}) = \lim_{t\to\infty} q_k(\mathbf{x}; t)$ and therefore provide a natural comparison to the splitting probabilities. We observe that short-time fluxes yield a more accurate directional estimate $\widehat{\mathbf{x}}_{\text{MLE}}(t)$ on the source compared with longer time fluxes or splitting probabilities. Motivated by this observation, we investigate simple recovery algorithms that use the directional information content in early receptor arrivals. One such mechanism is a simple polar averaging of receptor inputs, which provides an accurate estimate of source direction at short times. At later times, for which the signalling molecules have diffused far from the source, the estimate is no longer reliable.

To explain the accuracy of short-time estimates, we obtain in the case of equally space receptors a homogenization result in which the mixed boundary conditions (1.2b) are replaced by a uniform Robin condition $D\nabla p \cdot \mathbf{n} = \kappa p$ for $N \gg 1$. The obtained homogenization parameter

$$D\kappa^{-1} = -\frac{2}{N}\log\left(\frac{\varepsilon N}{4}\right) \quad (1.5)$$

results in a very accurate representation of the solution in the regime $\varepsilon \ll \sqrt{Dt} \ll 1$. The homogenized solution allows for identification of the timescale at which particle density becomes radially symmetric—the time after which no directional information is incident to the receptors.

Finally, as a theoretical limit on the directional information of short-time arrivals, we apply extreme value theory [36–38] to obtain the arrival time t_a and arrival angle θ_a of the first impact among M

independent particles released from the source. For a circular cell of radius $r_{\text{cell}} = 1$ centred at the origin and source at $\mathbf{x}_0 = R(\cos\theta_0, \sin\theta_0)$, we obtain that for $M \gg 1$, the arrival angle is normally distributed $\mathcal{N}(\theta_0, \sigma_{\theta_a}^2)$ where

$$\sigma_{\theta_a}^2(M, R) \propto \frac{R(1 - (1/R))^2}{\log M}. \tag{1.6}$$

The implication of (1.6) is that a single particle, travelling along a ballistic path from the source to a cell receptor [36,37], can yield an accurate estimate on the direction of the source. Moreover, this estimate can be formed without a cell integrating receptor fluxes as required in the use of splitting probabilities or MLE. Finally, in §5, we conclude by discussing some potential extensions.

2. Asymptotic construction of splitting probabilities and dynamic fluxes

In this section, we obtain an asymptotic representation [17,23,35,39–41] of the solution of (1.1) and (1.2) as $\varepsilon \to 0$. This analysis requires knowledge of the solution $v_c(\mathbf{y})$ to a rescaled form of the governing equations in a stretched region $\mathbf{y} = (\mathbf{x} - \mathbf{x}_k)/\varepsilon$ in the vicinity of each receptor. The details of this solution are provided in appendix A. We consider the static and dynamic problems separately.

2.1. Splitting probabilities: the static problem

The splitting probabilities have previously been calculated for closed geometries ([17], Section 5) and here we modify the analysis for the exterior setting. The absorbers satisfy $\partial\Omega_j \to \mathbf{x}_j$ as $\varepsilon \to 0$. In terms of the local problem with stretched variable $\mathbf{y} = (\mathbf{x} - \mathbf{x}_j)/\varepsilon$, we establish that $\phi_k(\mathbf{x}_j + \varepsilon\mathbf{y}) \sim \delta_{jk} + A_{jk}\nu_j v_c(\mathbf{y})$ where v_c solves (A 2). This forms the local condition

$$\phi_k(\mathbf{x}) \sim \delta_{jk} + A_{jk}\nu_j \log|\mathbf{x} - \mathbf{x}_j| + A_{jk} + \cdots, \quad \mathbf{x} \to \mathbf{x}_j, \; j = 1, \ldots, N; \; \nu_j = \frac{-1}{\log(\varepsilon\ell_j/4)}.$$

In order to evaluate the limiting behaviour of (1.1) as $\varepsilon \to 0$, we may formally expand the solution in an asymptotic expansion of the small parameter $1/|\log\varepsilon|$ as

$$\left. \begin{array}{l} \phi_k(\mathbf{x}) = \phi_k^{(0)}(\mathbf{x}) + \frac{1}{|\log\varepsilon|}\phi_k^{(1)}(\mathbf{x}) + \mathcal{O}\left(\frac{1}{|\log\varepsilon|^2}\right) \\[2mm] dA_{jk} = A_{jk}^{(0)} + \frac{1}{|\log\varepsilon|}A_{jk}^{(1)} + \mathcal{O}\left(\frac{1}{|\log\varepsilon|^2}\right). \end{array} \right\} \tag{2.1}$$

and

After collecting terms, we have a series of problems. At leading order term, $\phi_k^{(0)}(\mathbf{x})$ satisfies

$$\Delta\phi_k^{(0)} = 0, \quad \mathbf{x} \in \mathbb{R}^2\backslash\Omega; \; \phi_k^{(0)}(\mathbf{x}) \text{ bounded as } |\mathbf{x}| \to \infty; \tag{2.2a}$$

$$\nabla\phi_k^{(0)} \cdot \mathbf{n} = 0, \quad \mathbf{x} \in \partial\Omega\backslash\cup_{j=1}^{N}\{\mathbf{x}_j\} \tag{2.2b}$$

and

$$\phi_k^{(0)}(\mathbf{x}) \sim \delta_{jk} + A_{jk}^{(0)} \quad \text{as } \mathbf{x} \to \mathbf{x}_j, \; j = 1, \ldots, N, \tag{2.2c}$$

while the correction problem for $\phi_k^{(1)}(\mathbf{x})$ satisfies

$$\Delta\phi_k^{(1)} = 0, \quad \mathbf{x} \in \mathbb{R}^2\backslash\Omega; \; \phi_k^{(1)}(\mathbf{x}) \text{ bounded as } |\mathbf{x}| \to \infty; \tag{2.3a}$$

$$\nabla\phi_k^{(1)} \cdot \mathbf{n} = 0, \quad \mathbf{x} \in \partial\Omega\backslash\cup_{j=1}^{N}\{\mathbf{x}_j\} \tag{2.3b}$$

and

$$\phi_k^{(1)}(\mathbf{x}) \sim A_{jk}^{(0)} \log|\mathbf{x} - \mathbf{x}_j| + A_{jk}^{(1)} - \log\frac{\ell_j}{4} \quad \text{as } \mathbf{x} \to \mathbf{x}_j, \; j = 1, \ldots, N, \tag{2.3c}$$

where the constants $A_{jk}^{(0)}$ and $A_{jk}^{(1)}$ are to be determined. We define the surface Green's function $G_s(\mathbf{x}; \boldsymbol{\xi})$ for the Laplacian, which solves

$$\Delta G_s = 0, \quad \mathbf{x} \in \mathbb{R}^2\backslash\Omega; \; -\nabla G_s \cdot \mathbf{n} = \delta(\mathbf{x} - \boldsymbol{\xi}), \; \mathbf{x} \in \partial\Omega\backslash\{\boldsymbol{\xi}\} \tag{2.4a}$$

and

$$G_s \sim \frac{-1}{\pi}\log|\mathbf{x} - \boldsymbol{\xi}| + R_s(\boldsymbol{\xi}) + o(1), \quad \text{as } \mathbf{x} \to \boldsymbol{\xi}. \tag{2.4b}$$

The leading order problem (2.2) has a constant solution while $\phi_k^{(1)}(\mathbf{x})$ is expressed as

$$\phi_k^{(1)}(\mathbf{x}) = -\pi \sum_{j=1}^{N} A_{jk}^{(0)} G_s(\mathbf{x}; \mathbf{x}_j) + \bar{\phi}_k^{(1)}, \tag{2.5}$$

for constant $\bar{\phi}_k^{(1)}$. So that there is no growth as $|\mathbf{x}| \to \infty$, we have that $\sum_{j=1}^{N} A_{jk}^{(0)} = 0$. This boundedness criteria is analogous to the Fredholm solvability condition used in the splitting problem on a finite domain [17]. Summing (2.2c) and applying $\sum_{j=1}^{N} A_{jk}^{(0)} = 0$ yields that

$$\phi_k^{(0)} = \frac{1}{N}, \quad A_{jk}^{(0)} = \frac{1}{N} \begin{cases} 1 - N & j = k \\ 1 & j \neq k \end{cases}. \tag{2.6}$$

The equality of the splitting probabilities in the limit $\varepsilon \to 0$ means that the finite receptor size is necessary to perform source inference in two dimensions. This is in contrast to the three-dimensional equivalent [21]. Matching the solution (2.5) to local behaviour (2.3c) yields $(N+1)$ linear equations for the values of the constants $(A_{1k}^{(1)}, \ldots, A_{Nk}^{(1)}, \bar{\phi}_k^{(1)})$,

$$\sum_{j=1}^{N} A_{jk}^{(1)} = 0, \quad \bar{\phi}_k^{(1)} - \pi \left[A_{jk}^{(0)} R_s(\mathbf{x}_j) + \sum_{i=1 i \neq j}^{N} A_{ik}^{(0)} G_s(\mathbf{x}_i, \mathbf{x}_j) \right] = A_{jk}^{(1)} - \log \frac{\ell_j}{4}, \quad j = 1, \ldots, N.$$

This completes the expansion to $\mathcal{O}(|\log \varepsilon|^{-1})$. Further terms of the expansion can be calculated to improve the accuracy of the series; however, these additional terms cannot mitigate the fact that $1/|\log \varepsilon|^{n+1} \ll 1/|\log \varepsilon|^{n}$ only when ε is exceedingly small. This well-known issue of logarithmic expansions in two-dimensional singularly perturbed problems [39,42] can be resolved by obtaining the so-called 'sums-of-logs' solution to (1.1). This involves positing the expansion

$$\phi_k(\mathbf{x}) = \phi_k^*(\mathbf{x}; \boldsymbol{\nu}) + o(1), \quad \text{as } \varepsilon \to 0,$$

where the correction terms are smaller than any power of $1/|\log \varepsilon|$. Here, $\phi^*_k(\mathbf{x}; \boldsymbol{\nu})$ satisfies

$$\Delta \phi_k^* = 0, \quad \mathbf{x} \in \mathbb{R}^2 \backslash \Omega; \quad \phi_k^*(\mathbf{x}) \text{ bounded as } |\mathbf{x}| \to \infty; \tag{2.7a}$$

$$\nabla \phi_k^* \cdot \mathbf{n} = 0, \quad \mathbf{x} \in \partial\Omega \backslash \cup_{j=1}^{N} \{\mathbf{x}_j\} \tag{2.7b}$$

and
$$\phi_k^*(\mathbf{x}) \sim \delta_{jk} + A_{jk} \nu_j \log|\mathbf{x} - \mathbf{x}_j| + A_{jk}, \quad \text{as } \mathbf{x} \to \mathbf{x}_j, \ j = 1, \ldots, N. \tag{2.7c}$$

In terms of the surface Green's function, the solution of (2.7) is expressed as the linear combination

$$\phi_k^*(\mathbf{x}) = -\pi \sum_{j=1}^{N} A_{jk} \nu_j G_s(\mathbf{x}; \mathbf{x}_j) + \bar{\phi}_k, \tag{2.8}$$

where $\bar{\phi}_k = \lim_{|\mathbf{x}| \to \infty} \phi_k^*(\mathbf{x})$ is a constant arising from the homogeneous solution which reflects the splitting probability independent of the initial location. The solution (2.8) must not contribute a monopole as $|\mathbf{x}| \to \infty$ and so the strength terms $\{\nu_j A_{jk}\}_{j=1}^{N}$ sum to zero, which enforces that $\phi^*_k(\mathbf{x}) \in (0, 1)$ for all $\mathbf{x} \in \mathbb{R}^2 \backslash \Omega$. The additional constraints for the unknowns $(A_{1k}, \ldots, A_{Nk}, \bar{\phi}_k)$ arise from matching the solution (2.8) to the local behaviour (2.7c). In total, the system of $(N+1)$ linear equations becomes

$$\sum_{j=1}^{N} \nu_j A_{jk} = 0, \quad \bar{\phi}_k - \pi \left[A_{jk} \nu_j R_s(\mathbf{x}_j) + \sum_{\substack{i=1 \\ i \neq j}}^{N} A_{ik} \nu_i G_s(\mathbf{x}_i, \mathbf{x}_j) \right] = A_{jk} + \delta_{jk}, \quad j = 1, \ldots, N.$$

This system is compactly represented in matrix form as

$$\begin{bmatrix} \mathcal{I} + \pi \mathcal{G}_s \mathcal{V} & -\mathbf{e}^T \\ \boldsymbol{\nu} & 0 \end{bmatrix} \begin{bmatrix} \mathbf{A}_k \\ \bar{\phi}_k \end{bmatrix} = - \begin{bmatrix} \mathbf{e}_k \\ 0 \end{bmatrix}, \quad \begin{matrix} \mathbf{A}_k = (A_{1k}, \ldots, A_{Nk}), \\ \boldsymbol{\nu} = (\nu_1, \ldots, \nu_N) \end{matrix} \tag{2.9a}$$

and

$$\begin{matrix} \mathbf{e} = (1, 1, \ldots, 1), \\ \mathbf{e}_k = (0, \ldots \underbrace{1}_{k^{\text{th}}} \ldots, 0), \end{matrix} \quad [\mathcal{G}_s]_{i,j} = \begin{cases} R_s(\mathbf{x}_i) & i = j \\ G_s(\mathbf{x}_i; \mathbf{x}_j) & i \neq j \end{cases} \quad [\mathcal{V}]_{i,j} = \begin{cases} \nu_i & i = j \\ 0 & i \neq j \end{cases} \tag{2.9b}$$

and $\mathcal{I}$ is the $N \times N$ identity matrix. This linear system is solved and the full solution obtained from (2.8). In appendix B, we give derivations of Green's functions $G_s(\mathbf{x}; \boldsymbol{\xi})$ for the disc and half-plane geometries.

2.2. Receptor arrival statistics: the dynamic problem

To obtain the dynamic quantities (1.3), we proceed by applying a 'hybrid numerical-asymptotic' method [35,41] to the parabolic problem (1.2). The steps of this method are to first apply a Laplace transform to the underlying parabolic equation, following by matched asymptotic solution of the elliptic transform problem. Finally, the Laplace transform is inverted numerically in terms of an efficient quadrature of the Bromwich contour. Our goal is to obtain the dynamic quantities

$$
\mathcal{J}_k(t) = -D \int_{\partial \Omega_k} \nabla p \cdot \mathbf{n} \, dS, \quad q_k(t) = \frac{\int_0^t \mathcal{J}_k(\tau) \, d\tau}{\int_0^t \rho(\tau), \, d\tau}, \quad k = 1, \ldots, N. \tag{2.10}
$$

Accordingly, we define the Laplace transform of $p(\mathbf{x}, t)$

$$
\hat{p}(\mathbf{x}; s) = \int_{t=0}^{\infty} p(\mathbf{x}, t) \, e^{-st} \, dt, \tag{2.11}
$$

where $p(\mathbf{x}, t)$ satisfies (1.2) and the transform $\hat{p}(\mathbf{x}; s)$ solves the modified Helmholtz equation

$$
D\Delta \hat{p} - s\hat{p} = -\delta(\mathbf{x} - \mathbf{x}_0), \quad \mathbf{x} \in \mathbb{R}^2 \backslash \Omega; \tag{2.12a}
$$

$$
\hat{p} = 0, \quad \mathbf{x} \in \partial \Omega_a; \qquad D\nabla \hat{p} \cdot \mathbf{n} = 0, \quad \mathbf{x} \in \partial \Omega_r. \tag{2.12b}
$$

Following the hybrid-asymptotic approach [35,43], we solve (2.12) by means of matched asymptotic expansion in the limit $\varepsilon \to 0$ and as such, replace each absorbing site $\partial \Omega_j$ with the local behaviour $\hat{p} \sim A_j(s)\nu_j \log |\mathbf{x} - \mathbf{x}_j| + A_j(s)$ as $\mathbf{x} \to \mathbf{x}_j$. In this boundary layer analysis for the dynamic problem, we assume that $\varepsilon^2 s \ll 1$. Therefore, our results are not uniformly valid as $s \to \infty$, or correspondingly $t \to 0$. The expansion $\hat{p}(\mathbf{x}) = \hat{p}^*(\mathbf{x}; \nu, s) + o(1)$ results in a problem which again 'sums-the-logs' where $\hat{p}^*$ solves

$$
D\Delta \hat{p}^* - s\hat{p}^* = -\delta(\mathbf{x} - \mathbf{x}_0), \quad \mathbf{x} \in \mathbb{R}^2 \backslash \Omega; \quad D\nabla \hat{p}^* \cdot \mathbf{n} = 0, \quad \mathbf{x} \in \partial \Omega \backslash \cup_{j=1}^N \{\mathbf{x}_j\} \tag{2.13a}
$$

and

$$
\hat{p}^*(\mathbf{x}) \sim A_j(s)\nu_j \log |\mathbf{x} - \mathbf{x}_j| + A_j(s), \quad \text{as } \mathbf{x} \to \mathbf{x}_j, \ j = 1, \ldots, N. \tag{2.13b}
$$

The general solution of (2.13) is developed as

$$
\hat{p}^*(\mathbf{x}) = G_h(\mathbf{x}; \mathbf{x}_0, s) - \pi D \sum_{j=1}^N A_j(s)\nu_j G_h(\mathbf{x}; \mathbf{x}_j, s), \tag{2.14}
$$

where $G_h(\mathbf{x}; \boldsymbol{\xi}, s)$ is Green's function of the modified Helmholtz equation satisfying

$$
D\Delta G_h - sG_h = 0, \quad \mathbf{x} \in \mathbb{R}^2 \backslash \Omega; \quad -D\nabla G_h \cdot \mathbf{n} = \delta(\mathbf{x} - \boldsymbol{\xi}), \quad \mathbf{x} \in \partial \Omega \backslash \{\boldsymbol{\xi}\} \tag{2.15a}
$$

and

$$
G_h \sim \frac{-1}{\pi D} \log |\mathbf{x} - \boldsymbol{\xi}| + R_h(\boldsymbol{\xi}; s) + o(1), \quad \text{as } \mathbf{x} \to \boldsymbol{\xi}. \tag{2.15b}
$$

In appendix B, we derive expressions for solutions of (2.15) in the upper half-plane and the disc exterior geometries. Matching (2.14) to the local condition (2.13b) as $\mathbf{x} \to \mathbf{x}_k$ yields the conditions

$$
G_h(\mathbf{x}_k; \mathbf{x}_0, s) = A_k(s) + \pi D \left[A_k(s) R_h(\mathbf{x}_k) + \sum_{\substack{j=1 \\ j \neq k}}^N A_j(s)\nu_j G_h(\mathbf{x}_k; \mathbf{x}_j, s) \right], \tag{2.16a}
$$

for $k = 1, \ldots,$ PON. In terms of the strength vector $\mathbf{A}(s) = [A_1(s), \ldots, A_N(s)]^T$, equations (2.16a) can be represented in matrix equation form where the strengths satisfy the linear system,

$$
(\mathcal{I} + \pi D \mathcal{G}_h \mathcal{V}) \mathbf{A}(s) = \mathbf{g}_0, \quad [\mathcal{G}_h]_{i,j} = \begin{cases} R_h(\mathbf{x}_i; s) & i = j \\ G_h(\mathbf{x}_i; \mathbf{x}_j, s) & i \neq j \end{cases}, \quad \mathbf{g}_0 = \begin{bmatrix} G_h(\mathbf{x}_1; \mathbf{x}_0, s) \\ \vdots \\ G_h(\mathbf{x}_N; \mathbf{x}_0, s) \end{bmatrix}. \tag{2.16b}
$$

In the system (2.16b), the vector $\mathbf{g}_0$ describes the interaction between the source location and each receptor while the matrix $\mathcal{G}_h$ encodes global information on the receptor configuration. We remark that in the vector $\mathbf{g}_0$, Green's function is evaluated for a source in the bulk, while for the entries of $\mathcal{G}_h$ each source
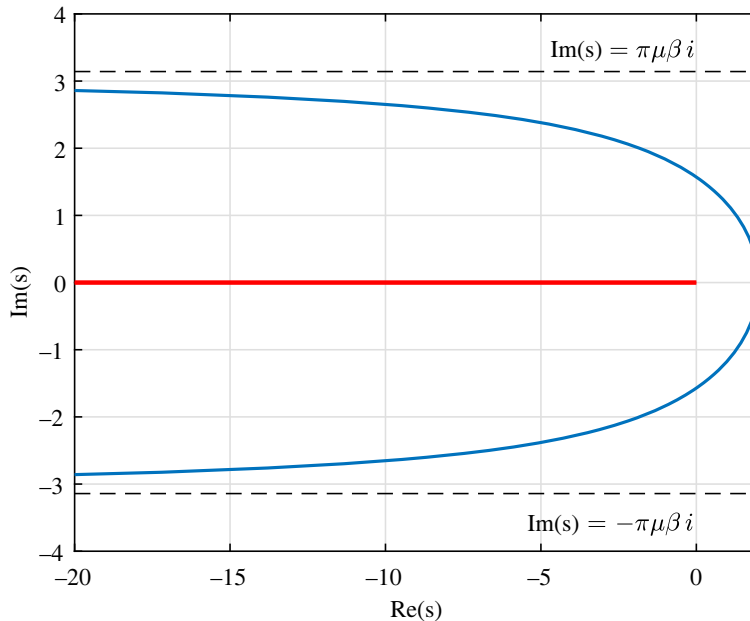
Figure 2. A schematic of the Talbot curve (2.19) for parameter values $\sigma = 0$, $\mu = 2$, $\beta = 0.5$. The red line indicates the singularities along the negative real line arising from the $\sqrt{s}$ singularity.

is on the surface $\partial \Omega$. Therefore, we must obtain $G_h(\mathbf{x}; \boldsymbol{\xi}, s)$ for both $\boldsymbol{\xi} \in \partial \Omega$ and $\boldsymbol{\xi} \in \mathbb{R}^2 \setminus \Omega$ separately. The geometric information of each receptor (e.g. size) is encoded solely through the diagonal matrix $\mathcal{V}$, defined in (2.9b).

In this section, we show how to extend this asymptotic analysis to obtain the full time-dependent arrival statistics. After applying the Laplace transform $\hat{p}(\mathbf{x}; s) = \int_{t=0}^{\infty} e^{-st} p(\mathbf{x}; t) \, dt$ to (1.2), we obtain the modified Helmholtz problem (2.12). We now discuss the inversion from Laplace space to physical time. One quantity of interest is the flux (1.3) through each of the receptors. In the transform variables, these quantities are

$$\widehat{\mathcal{J}}_k(s) = \pi D A_k(s) v_k. \tag{2.17}$$

From the solution of the linear system (2.16b), we then apply a numerical inverse Laplace transform [44–46] to obtain the fluxes over each receptor (2.17). Numerical inverse Laplace transform is based on quadrature of the Bromwich integral, specifically

$$\mathcal{J}_k(t) = \frac{1}{2\pi i} \int_{\Gamma_B} e^{st} \widehat{\mathcal{J}}_k(s) \, ds, \tag{2.18}$$

where Γ_B is the complex contour $\Gamma_B = \{\gamma + iy \mid -\infty < y < \infty\}$. The parameter γ is chosen so that all singularities of $\widehat{\mathcal{J}}_k(s)$ lie to the left of $\mathrm{Re}(s) = \gamma$. In the present scenario associated with diffusion, the singularities of $\widehat{\mathcal{J}}_k(s)$ lie along the negative real axis arising from the branch cut of $\sqrt{s}$. Rapid and effective numerical evaluation of (2.18) is achieved by deforming the contour around $\mathrm{Re}(s) = 0$ such that the integrand of (2.18) decays very rapidly for $\mathrm{Re}(s) < 0$. The Talbot contour Γ_T is a family of deformations (figure 2) to Γ_B given parametrically by

$$\Gamma_T = \{\sigma + \mu(\theta \cot \theta + \beta i \, \theta) \mid -\pi < \theta < \pi\}, \tag{2.19}$$

where σ, μ and β are shape parameters [44,47]. To achieve rapid and accurate evaluation of the inverse Laplace transform, we apply the midpoint rule to the integral (2.18) along the curve (2.19).

2.3. Homogenization

In this section, we identify a *boundary homogenization* limit as $N \to \infty$ that replaces the mixed Neumann and Dirichlet boundary conditions by a single condition $D\nabla p_h \cdot \mathbf{n} = \kappa p_h$ for a permeability parameter $\kappa > 0$ [31,48–53]. For a circular cell Ω of radius $r_{\mathrm{cell}} = 1$ centred at the origin with source $\mathbf{x}_0 = R \, e^{i\theta_0}$, the

homogenized problem $p_h(r, \theta, t; R)$ solves

$$\frac{\partial p_h}{\partial t} = D\left[\frac{\partial^2 p_h}{\partial r^2} + \frac{1}{r}\frac{\partial p_h}{\partial r} + \frac{1}{r^2}\frac{\partial^2 p_h}{\partial \theta^2}\right], \quad r > 1, \quad \theta \in (0, 2\pi), \quad t > 0; \tag{2.20a}$$

$$p_h = \frac{1}{r}\delta(r - R)\delta(\theta - \theta_0), \quad r > 1, \quad \theta \in (0, 2\pi), \quad t = 0; \tag{2.20b}$$

$$p_h(r, \theta + 2\pi, t) = p_h(r, \theta, t), \quad r > 1, \quad \theta \in (0, 2\pi), \quad t > 0 \tag{2.20c}$$

and
$$D\frac{\partial p_h}{\partial r} = \kappa p_h, \quad r = 1, \quad \theta \in (0, 2\pi), \quad t > 0. \tag{2.20d}$$

We find in appendix B that the surface flux $\mathcal{J}(\theta, t) = D\partial_r p_h \mid_{r=1}$ of (2.20) has Laplace transform

$$\widehat{\mathcal{J}}(\theta, s) = \frac{1}{2\pi}\chi_0(\alpha) + \frac{1}{\pi}\sum_{m=1}^{\infty}\chi_m(\alpha)\cos m(\theta - \theta_0), \quad \chi_m(\alpha) = \frac{K_m(\alpha R)}{K_m(\alpha) - D\kappa^{-1}\alpha K_m'(\alpha)}, \tag{2.21}$$

where $K_m(z)$ is the modified Bessel function of order m and $\alpha = \sqrt{s/D}$ is the scaled Laplace parameter. To derive a formula for κ, we consider N equally spaced receptors of common angular extent ε with complex coordinates $\mathbf{x}_j = e^{i\theta_j}$ for $\theta_j = 2\pi j/N$ and $j = 1, \ldots, N$. For the strength vector $\mathbf{A}(s) = [A_1(s), \ldots, A_N(s)]^T$, we define the surface flux

$$\widehat{\mathcal{J}}_N(\theta, s) = \sum_{j=1}^{N}\widehat{\mathcal{J}}_k(s)\delta(\theta - \theta_j) = \pi D\nu\sum_{j=1}^{N}A_j(s)\delta(\theta - \theta_j).$$

The flux, $\widehat{\mathcal{J}}_N(\theta, s)$, in this asymptotic limit is a sum of N δ-functions, one for each receptor, and we wish to study how this measure converges to the homogenized flux $\widehat{\mathcal{J}}(\theta, s)$. What we will demonstrate is that as $N \to \infty$ the coefficients in the Fourier series of $\widehat{\mathcal{J}}_N(\theta, s)$ converge to those of the Fourier cosine series for $\widehat{\mathcal{J}}(\theta, s)$ given by (2.21). We now solve for the fluxes explicitly using ideas from the discrete Fourier transform [54].

The Green's function matrix $\mathcal{G}_h$ defined in (2.16a) is circulant, therefore we can find an eigenbasis $\{\mathbf{u}_1, \ldots, \mathbf{u}_N\}$ such that

$$\mathbf{u}_m \equiv [1, \omega_m, \omega_m^2, \ldots, \omega_m^{N-1}]^T = [1, \omega_m, \omega_{2m}, \ldots, \omega_{(N-1)m}]^T, \quad \omega_k = e^{2\pi i k/M}. \tag{2.22}$$

Expanding the strength vector as

$$\mathbf{A}(s) = \sum_{m=1}^{N}c_m\mathbf{u}_m,$$

guarantees due to orthogonality that $c_q = (1/N)\mathbf{u}_q^* \cdot \mathbf{A}(s)$, which we expand for later use as

$$e^{iq\theta_0}c_q = e^{iq\theta_0}\frac{1}{N}\sum_{j=1}^{N}A_j(s)e^{-iq\theta_j} = \frac{1}{N}\sum_{j=1}^{N}A_j(s)[\cos q(\theta_j - \theta_0) - i\sin q(\theta_j - \theta_0)]. \tag{2.23}$$

Taking the inner-product of (2.16b) with $\mathbf{u}_q^*$ yields that

$$c_q = \frac{\mathbf{u}_q^* \cdot \mathbf{g}_0}{N + \pi D\nu \mathbf{u}_q^* \mathcal{G}_h \mathbf{u}_q}. \tag{2.24}$$

For the terms $\mathbf{u}_q^* \mathcal{G}_h \mathbf{u}_q$, we need the surface Green's function (appendix B)

$$G_h(\mathbf{x}; \boldsymbol{\xi}, s) = -\frac{1}{\pi D}\log|\mathbf{x} - \boldsymbol{\xi}| + R_h(\mathbf{x}; \boldsymbol{\xi}, s) \tag{2.25a}$$

and

$$R_h(\mathbf{x}; \boldsymbol{\xi}, s) = \frac{1}{\pi D}\left(-\frac{1}{2}\frac{K_0(\alpha)}{\alpha K_0'(\alpha)} - \sum_{m=1}^{\infty}\left[\frac{K_m(\alpha)}{\alpha K_m'(\alpha)} + \frac{1}{m}\right]\cos m(\theta - \theta_0)\right). \tag{2.25b}$$

where $\mathbf{x} = e^{i\theta}$ and $\boldsymbol{\xi} = e^{i\theta_0}$. We decompose $\mathbf{u}_q^* \mathcal{G}_h \mathbf{u}_q = \mathcal{S} + \mathcal{R}$ where the regular term $\mathcal{R}$ is

$$\begin{aligned}
\mathcal{R} &= \sum_{m=1}^{N}\sum_{n=1}^{N} e^{-iq(\theta_m - \theta_0)} R_h(\mathbf{x}_m; \mathbf{x}_n) e^{iq(\theta_n - \theta_0)} \\
&= \left(\frac{N}{2\pi}\right)^2 \int_{\theta=0}^{2\pi}\int_{\bar{\theta}=0}^{2\pi} e^{-iq(\theta - \theta_0)} R_h(\mathbf{x}(\theta); \mathbf{x}(\bar{\theta})) e^{iq(\theta - \bar{\theta})} \, d\theta \, d\bar{\theta} + \text{H.O.T.}
\end{aligned} \tag{2.26}$$

$$= -\frac{N^2}{2\pi D} \begin{cases} \frac{K_0(\alpha)}{\alpha K_0'(\alpha)}, & q = 0; \\ \frac{K_q(\alpha)}{\alpha K_q'(\alpha)} + \frac{1}{q}, & q = 1, 2, 3, \ldots \end{cases} \tag{2.27}$$

The singular term $\mathcal{S}$ is calculated as

$$\begin{aligned}
\mathcal{S} &= -\frac{1}{\pi D}\sum_{m=1}^{N}\sum_{n=1, n \neq m}^{N} e^{-iq(\theta_m - \theta_n)} \log|\mathbf{x}_m - \mathbf{x}_n| = -\frac{N}{\pi D}\sum_{n=2}^{N}\cos(q\theta_n)\log|\mathbf{x}_n - 1| \\
&= -\frac{N}{\pi D}\log N - \frac{N}{\pi D}\sum_{n=1}^{N}(\cos(q\theta_n) - 1)\log|\mathbf{x}_n - 1| \\
&= -\frac{N}{\pi D}\log N + \frac{N^2}{2\pi^2 D}\int_{\theta=0}^{2\pi}(1 - \cos(q\theta))\log\left(2\sin\frac{\theta}{2}\right)d\theta + \text{H.O.T.} \\
&= -\frac{N}{\pi D}\log N + \frac{N^2}{2\pi D}\begin{cases} 0, & q = 0; \\ \frac{1}{q}, & q = 1, 2, 3, \ldots \end{cases}
\end{aligned} \tag{2.28}$$

In the above calculations, higher-order terms (H.O.T.) arise by interpreting summations as quadratures and replacing with the equivalent integrals, a technique familiar from the discrete Fourier transform [54]. In practice, for a fixed wavenumber (here q) as N increases the error drops exponentially in $1/N$ for C^∞ integrands.

Combining (2.27) and (2.28) gives

$$\mathbf{u}_q^* \mathcal{G}_h \mathbf{u}_q = \mathcal{R} + \mathcal{S} = -\frac{N\log N}{\pi D} - \frac{N^2}{2\pi D}\frac{K_q(\alpha)}{\alpha K_q'(\alpha)}. \tag{2.29}$$

To calculate the term $\mathbf{u}_q^* \cdot \mathbf{g}_0$, we need the bulk Green's function (B 8)

$$G_h(\theta; R, \theta_0, s) = -\frac{1}{2\pi D}\frac{K_0(\alpha R)}{\alpha K_0'(\alpha)} - \frac{1}{\pi D}\sum_{m=1}^{\infty}\frac{K_m(\alpha R)}{\alpha K_m'(\alpha)}\cos m(\theta - \theta_0), \tag{2.30}$$

for $\mathbf{x} = (\cos\theta, \sin\theta)$ and $\boldsymbol{\xi} = R(\cos\theta_0, \sin\theta_0)$. We calculate that

$$\begin{aligned}
\mathbf{u}_q^* \cdot \mathbf{g}_0 &= \sum_{k=1}^{N} e^{-iq\theta_k} G_h(\mathbf{x}_k, \mathbf{x}_0, s) \approx e^{-iq\theta_0}\frac{N}{2\pi}\int_{\theta=0}^{2\pi}\cos q(\theta - \theta_0) G_h(\theta; R, \theta_0) \, d\theta \\
&= -e^{-iq\theta_0}\frac{N}{2\pi D}\frac{K_q(\alpha R)}{\alpha K_q'(\alpha)} + \text{H.O.T.}
\end{aligned} \tag{2.31}$$

Combining equations (2.24), (2.29) and (2.31), we determine that

$$c_q = \frac{\mathbf{u}_q^* \cdot \mathbf{g}_0}{N + \pi D\nu \, \mathbf{u}_q^* \mathcal{G}_h \mathbf{u}_q} \approx \frac{e^{-iq\theta_0}}{\pi D\nu N}\frac{(K_q(\alpha R)/\alpha K_q'(\alpha)).}{(2/N)\log(\varepsilon N/4) + (K_q(\alpha)/\alpha K_q'(\alpha))}. \tag{2.32}$$

If we now formally expand $\widehat{\mathcal{J}}_N(\theta, s)$ as a Fourier series,

$$\widehat{\mathcal{J}}_N(\theta, s) = \frac{1}{2\pi}\overline{\chi}_0(\alpha) + \frac{1}{\pi}\sum_{m=1}^{\infty}\overline{\chi}_m(\alpha)\cos m(\theta - \theta_0) + \overline{\psi}_m(\alpha)\sin m(\theta - \theta_0), \tag{2.33}$$

we find that for $m = 0, 1, 2, \ldots,$

$$\overline{\chi}_m(\alpha) = \int_0^{2\pi} \widehat{\mathcal{J}}_N(\theta, s) \cos m(\theta - \theta_0) \, \mathrm{d}\theta = \int_0^{2\pi} \left[\sum_{j=1}^N \widehat{\mathcal{J}}_k(s) \delta(\theta - \theta_j) \right] \cos m(\theta - \theta_0) \, \mathrm{d}\theta,$$

$$= \sum_{j=1}^N \widehat{\mathcal{J}}_k(s) \cos m(\theta_j - \theta_0),$$

$$= \pi D\nu \sum_{j=1}^N A_j(s) \cos m(\theta_j - \theta_0).$$

A similar calculation yields for $m = 1, 2, \ldots$ that $\overline{\psi}_m(\alpha) = \pi D\nu \sum_{j=1}^N A_j(s) \sin m(\theta_j - \theta_0)$. Now combining this calculation with (2.23) yields

$$e^{iq\theta_0} c_q = \frac{1}{N} \sum_{j=1}^N A_j [\cos q(\theta_j - \theta_0) - i \sin q(\theta_j - \theta_0)] = \frac{1}{\pi D\nu N} [\overline{\chi}_m(\alpha) - i\overline{\psi}_m(\alpha)], \tag{2.34}$$

but from (2.32) this yields in the limit of large N (and fixed q) that

$$\overline{\chi}_q(\alpha) - i\overline{\psi}_q(\alpha) \sim \frac{K_q(\alpha R)/\alpha K_q'(\alpha)}{(2/N) \log(\varepsilon N/4) + (K_q(\alpha)/\alpha K_q'(\alpha))},$$

and as the right-hand side is real, we conclude that $\overline{\psi}_q(\alpha)$ tends to zero in the limit of large N. This can be interpreted physically as an approximately symmetric response to the source at θ_0 in the limit of large N. A direct comparison with the Robin surface flux (2.21) reveals that $\overline{\chi}_q(\alpha) = \chi_q(\alpha)$ (again in the limit of large N) if one chooses the homogenization parameter to be

$$D\kappa^{-1} = -\frac{2}{N} \log\left(\frac{\varepsilon N}{4}\right). \tag{2.35}$$

This result is in agreement with those previously determined for steady state [55,56] quantities, but is obtained here for all dynamic modes, demonstrating that homogenization has much broader efficacy. This has been recently observed in the first passage time distribution of capture to planar absorbers [35].

2.4. Short-time asymptotics via the method of moments

In this section, we obtain the short-time asymptotics for the solution of (2.20) which will be used to describe the source detection for very early arrivals to the cellular surface. This is a familiar problem from stochastic processes; the earliest arrivals are concentrated at the point closest to the source. Heuristically, this can be viewed as a boundary layer calculation. The outer solution is just the free space Green's function and the inner solution is confined to a boundary layer of width $\sqrt{Dt}$ at the edge of the disc. Specifically, we will consider the problem when $\varepsilon \ll \sqrt{Dt} \ll 1$, that is where the diffusion length is much longer than the typical receptor size (so the homogenization approximation is valid) but much smaller that the disc radius. We expect that the arrivals will be concentrated near the point on the disc closest to the source.

The homogenized problem derived in the previous section allows a straightforward characterization of the fluxes at short times via the method of moments. Our starting point is the expansion of the Laplace transform of the flux density (B 10) as a Fourier cosine series (reflecting the even symmetry of the distribution). For convenience, we take $\theta_0 = 0$ and calculate from (2.21) and the orthogonality of the Fourier modes that

$$\chi_n(\alpha) = \int_{\theta=-\pi}^{\pi} \widehat{\mathcal{J}}(\theta, \alpha) \cos n\theta \, \mathrm{d}\theta. \tag{2.36}$$

Next, we exploit the exponential localization of the distribution to treat the interval $\theta \in [-\pi, \pi]$ as effectively infinite and define the centred moments of the distribution, $M_n(t)$ and their Laplace transform $\widehat{M}_n(\alpha) = \mathcal{L}[M_n(t)]$, where as usual $\alpha = \sqrt{s/D}$,

$$M_n(t) = \int_{\theta=-\pi}^{\pi} \mathcal{J}(\theta, t) \theta^n \, \mathrm{d}\theta \quad \text{and} \quad \widehat{M}_n(\alpha) = \int_{\theta=-\pi}^{\pi} \widehat{\mathcal{J}}(\theta, \alpha) \theta^n \, \mathrm{d}\theta. \tag{2.37}$$

The linearity of the moments implies that the Laplace transform of the moments are the moments of the Laplace transform. The even symmetry guarantees that the odd moments will vanish, as does the mean and the skewness of the distribution.

The first moment is exactly $\chi_0(\alpha)$ which we will expand for $\alpha = \sqrt{s/D} \gg 1$ corresponding to $\sqrt{Dt} \ll 1$. In addition, we will make an assumption about the homogenization parameter that $0 < D\kappa^{-1} \ll 1$. This can be thought of as having a fixed receptor fraction on the surface, $\varepsilon N < 4$ (to ensure positivity of the log term), and letting N increase to infinity.

$$\widehat{M}_0(\alpha) = \chi_0(\alpha) = \frac{K_0(\alpha R)}{K_0(\alpha) - D\kappa^{-1}\alpha K_0'(\alpha)} \sim \frac{\kappa\, e^{-\alpha(R-1)}}{\sqrt{R}(\alpha D + \kappa)}\left[1 + \mathcal{O}\left(\frac{1}{\alpha}\right)\right],$$

whose inverse transform is

$$M_0(t) = \frac{\kappa}{\sqrt{R}}\, e^{-((R-1)^2/4Dt)}\left[\frac{1}{\sqrt{\pi Dt}} - \frac{\kappa}{D}\operatorname{erfc}(\beta)\, e^{\beta^2}\right]\cdot\left[1 + \mathcal{O}(\sqrt{Dt})\right] \quad \beta = \frac{2\kappa t + (R-1)}{2\sqrt{Dt}}.$$

Note that $\beta > (R-1)/2\sqrt{Dt} \gg 1$ and expanding in the limit of large β yields

$$M_0(t) = \frac{\kappa(R-1)}{\sqrt{R}}\frac{e^{-(R-1)^2/4Dt}}{\sqrt{\pi Dt}}\left[\frac{1}{2\kappa t + (R-1)}\right]\cdot\left[1 + \mathcal{O}(\sqrt{Dt})\right],$$

which is a uniform approximation independent of the relative sizes of κt and $(R-1)$.

Expanding $\cos n\theta = 1 - (n\theta)^2/2 + (n\theta)^4/24 + \cdots$ as a Taylor series yields

$$\chi_n(\alpha) = \int_{\theta=0}^{2\pi} \widehat{\mathcal{J}}(\theta, \alpha)\cos n\theta\, \mathrm{d}\theta = \widehat{M}_0(\alpha) - \frac{n^2}{2}\widehat{M}_2(\alpha) + \frac{n^4}{24}\widehat{M}_4(\alpha) + \cdots. \tag{2.38}$$

We now expand $\chi_n(\alpha)$ for fixed n and $\alpha \gg 1$, a limit for which uniform approximations are well known for the modified Bessel functions. First, we rewrite $\chi_n(\alpha)$ as

$$\chi_n(\alpha) = \frac{K_n(\alpha R)/K_n'(\alpha)}{K_n(\alpha)/K_n'(\alpha) - D\kappa^{-1}}.$$

Asymptotically the ratios of Bessel functions for fixed n and $\alpha \gg 1$ yields

$$\frac{K_n(\alpha R)}{K_n'(\alpha)} \sim \frac{e^{-\alpha(R-1)}}{R}\left[-1 + \frac{(4n^2 + 3)(R-1) + 4}{8R}\alpha^{-1}\right.$$
$$\left. + \frac{(-16n^4 + 8n^2 - 33)(R-1)^2 + (3n^2 - 72)(R-1) + (64n^2 - 48)}{128}\alpha^{-2} + \mathcal{O}(\alpha^{-3})\right],$$

where the denominator $K_n(\alpha)/K_n'(\alpha)$ can be expanded by setting $R = 1$ in this expression. The jth term for the expression in the square bracket is a polynomial in n of degree $2(j-1)$ times $\alpha^{-(j-1)}$. Substituting into the expression for $\chi_n(\alpha)$ and expanding for $\alpha \gg 1$ while allowing the relative size of α and D/κ to be arbitrary allows us to identify the Laplace transforms of the moments in (2.38),

$$\widehat{M}_0(\alpha) \sim \frac{\kappa\, e^{-\alpha(R-1)}}{\sqrt{R}(\alpha D + \kappa)}\left[1 + \mathcal{O}\left(\frac{1}{\alpha}\right)\right],$$

$$\widehat{M}_2(\alpha) \sim \frac{\kappa(R-1)\, e^{-\alpha(R-1)}}{\alpha R^{3/2}(\alpha D + \kappa)}\left[1 + \mathcal{O}\left(\frac{1}{\alpha}\right)\right]$$

and $\quad\widehat{M}_4(\alpha) \sim \frac{3\kappa(R-1)^2\, e^{-\alpha(R-1)}}{\alpha^2 R^{5/2}(\alpha D + \kappa)}\left[1 + \mathcal{O}\left(\frac{1}{\alpha}\right)\right].$

The inverse transform $\widehat{M}_2(\alpha)$ can be approximated for $\alpha, \beta \gg 1$ as

$$M_2(t) = M_0(t)\left[\frac{2Dt}{R}\right]\cdot\left[1 + \mathcal{O}(\sqrt{Dt})\right].$$

This allows us to compute the variance

$$\operatorname{Var}[\mathcal{J}(\theta, t)] \equiv \frac{M_2(t)}{M_0(t)} \sim \frac{2Dt}{R}.$$

A similar tedious calculation yields the result that

$$M_4(t) = M_0(t) \left[\frac{12(Dt)^2}{R^2} \right] \cdot \left[1 + \mathcal{O}(\sqrt{Dt}) \right],$$

and shows that the kurtosis satisfies

$$\mathrm{Kur}[\mathcal{J}(\theta, t)] \equiv \frac{M_4(t) \cdot M_0(t)}{[M_2(t)]^2} \sim 3 + \mathcal{O}(\sqrt{Dt}).$$

This is consistent with a Gaussian distribution, specifically, we have in the limit $t \to 0^+$ that

$$\mathcal{J}(\theta, t) \sim \frac{\mathcal{M}}{\sigma \sqrt{2\pi}} e^{-(\theta^2/2\sigma^2)}; \quad \sigma^2 = \mathrm{Var}[\mathcal{J}(\theta, t)] \sim \frac{2Dt}{R} \tag{2.39a}$$

and

$$\mathcal{M} = M_0(t) \sim \frac{\kappa(R-1)}{\sqrt{\pi R D t}} e^{-((R-1)^2/4Dt)} \left[\frac{1}{2\kappa t + (R-1)} \right]. \tag{2.39b}$$

We remark that the limiting behaviour of (2.39b) as $t \to 0^+$ is consistent with the short-time asymptotic of the survival probability derived in (B 12).

3. Source recovery

In this section, we investigate source inference using both dynamics fluxes (4.2) and splitting probabilities. We consider the situation where M particles are released from a location $\mathbf{x}_0$. The particles arrive at one of the N receptors with centres $\{\mathbf{x}_k\}_{k=1}^N$ and the counts at each being $\{c_k\}_{k=1}^N$ so that $\sum_{k=1}^N c_k = M$.

One potential avenue for formulating a problem for the source location $\mathbf{x}_0$ uses the discrete splitting probabilities c_k/M together with the asymptotic formulation (2.8). Assuming $\phi_k \approx c_k/M$ for M sufficiently large, and source location $\mathbf{x}_0$, this yields the system

$$\bar{\phi}_k - \frac{c_k}{M} = \pi \sum_{j=1}^N A_j \nu_j G_s(\mathbf{x}_0; \mathbf{x}_j), \quad k = 1, \ldots, N. \tag{3.1}$$

For the circular cellular geometry (cf. figure 1), it was shown in [18] that the system (3.1) generates a unique solution provided $N \geq 3$. In practice, the number of receptors may be large so that (3.1) is highly overdetermined thus limiting the practicality in source inference. We therefore consider the maximum-likelihood approach of [21] which adopts a probabilistic viewpoint to obtain a distribution for the source location given splitting probabilities and the receptor counts $\{c_k\}_{k=1}^N$. The multinomial likelihood function is given by

$$(q_1)^{c_1} \times (q_2)^{c_2} \times \cdots \times (q_N)^{c_N} = \prod_{k=1}^N (q_k)^{c_k},$$

where $q_k := q_k(\mathbf{x}; t)$ are the dynamic signals or, alternatively, the splitting probabilities $\phi_k(\mathbf{x}) = \lim_{t \to \infty} q_k(\mathbf{x}, t)$. For convenience, the negative log-likelihood is considered giving the estimator

$$\widehat{\mathbf{x}}_{\mathrm{MLE}}(t) = \arg\max_{\mathbf{x}} \mathcal{L}(\mathbf{x}; t) \quad \text{and} \quad \mathcal{L}(\mathbf{x}; t) = -\sum_{k=1}^N c_k \log[q_k(\mathbf{x}; t)]. \tag{3.2}$$

The use of a finite number of signalling particles ($M < \infty$) reflects a low concentration of chemoattractant and simultaneously the number M serves as a parameter for controlling noise of the receptor signal in the source inference process. To more precisely quantify the role of noise in the inference process, we consider the 'exact' landscape $\mathcal{L}^*$ defined as

$$\mathcal{L}^*(\mathbf{x}; \mathbf{x}_0, t) = -\sum_{k=1}^N q_k(\mathbf{x}_0, t) \log[q_k(\mathbf{x}, t)]. \tag{3.3}$$

In (3.3), the finite receptor counts c_k have been replaced by the exact relative fluxes $q_k(\mathbf{x}_0, t)$. While it may be feasible to implement MLE on the cellular level [57], here we use this methodology only as a map from the receptor configuration and input signal to a source estimate.
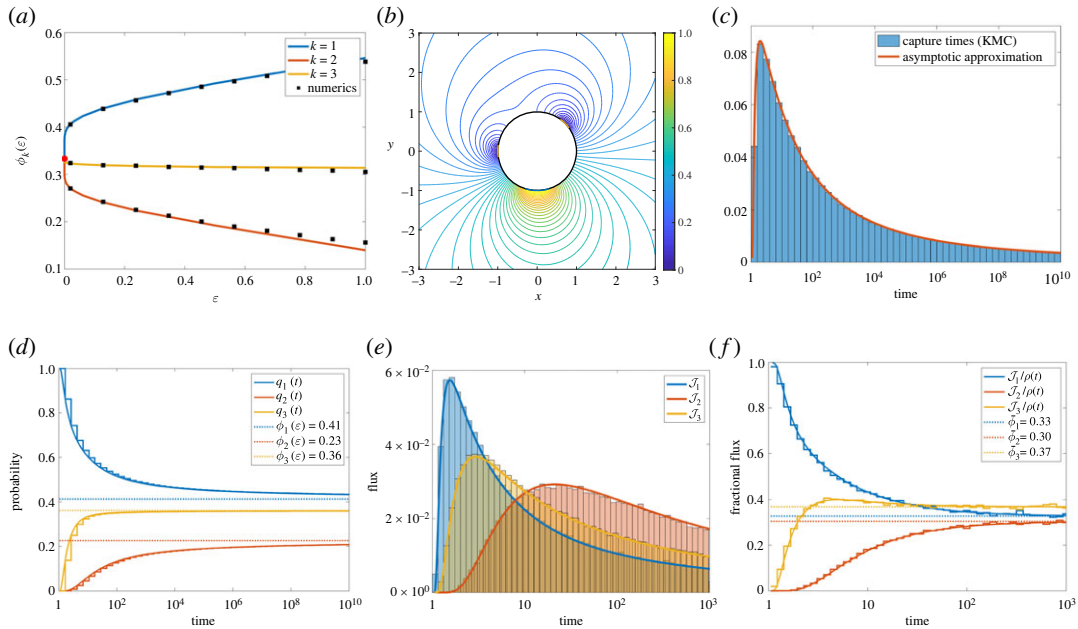
Figure 3. Validation of the hybrid asymptotic method for example 4.1 and parameters (4.1). Panels (a,b) feature numerical results from the series method described in appendix C while (c–f) feature $M = 10^6$ arrival times obtained from a kinetic Monte Carlo (KMC) method [35]. (a) Numerical validation of the asymptotic splitting probabilities. (b) Numerical solution of the splitting probability $\phi_3(\mathbf{x})$ for $\varepsilon = 0.3$. (c) Full distribution of first passage times from asymptotics (4.2) and KMC data. (d) Convergence of the accumulated signals (4.2) to the asymptotic splitting probabilities $\{\phi_1, \phi_2, \phi_3\}$ for $\varepsilon = 0.1$. (e) Fluxes $\mathcal{J}_k(t)$ against time to individual receptors. (f) Relative fluxes $\bar{\mathcal{J}}_k(t) = \mathcal{J}_k(t)/\rho(t)$ against time to individual receptors with convergence to $\{\bar{\phi}_1, \bar{\phi}_2, \bar{\phi}_3\}$.

4. Results

In this section, we provide validation of our results. We cross-verify where possible the different approaches to obtaining the static splitting probabilities and the dynamic receptor fluxes. In the static case of the splitting probabilities, we develop (see appendix C) a highly accurate numerical solution based on a least-squared fitting approach of (1.1). In all scenarios, a particle-based KMC method [35] is employed to rapidly and accurately sample all static and dynamic quantities while providing noisy receptor inputs for source reconstruction.

4.1. Example: asymptotic verification in disc geometry with three receptors

In this test case, we validate in figure 3 the asymptotic approximation on the disc geometry with three receptors given by parameters

$$\ell = \varepsilon \ell_c = \varepsilon \left[\frac{\pi}{3}, \frac{\pi}{3}, \frac{2\pi}{3} \right], \quad \mathbf{x}_j = [\cos \theta_j, \sin \theta_j], \quad \theta_j = \left[\frac{\pi}{4}, \pi, \frac{3\pi}{2} \right], \quad \mathbf{x}_0 = [2, 0]. \tag{4.1}$$

In figure 3a, we show that the splitting probabilities $\{\phi_1(\varepsilon), \phi_2(\varepsilon), \phi_3(\varepsilon)\}$ obtained from asymptotics and numerics are in very close agreement for a wide range of ε values. As $\varepsilon \to 0$, we observe that $\phi_k(\varepsilon) \to 1/N$ in agreement with equation (2.6). For the splitting probability $\phi_3(0.3)$, we show in figure 3b contours indicating equal likelihood of arriving first at receptor $k = 3$.

To validate the time-dependent arrival statistics, we calculate from (2.18) the full arrival density $\rho(t)$, the fractional cumulative signal $q_k(t)$ and the fractional fluxes $\bar{\mathcal{J}}_k(t)$ satisfying

$$\rho(t) = \sum_{j=1}^{N} \mathcal{J}_j(t), \quad q_k(t) = \frac{\int_0^t \mathcal{J}_k(\tau) \, d\tau}{\int_0^t \rho(\tau) \, d\tau} \quad \text{and} \quad \bar{\mathcal{J}}_k(t) = \frac{\mathcal{J}_k(t)}{\rho(t)}. \tag{4.2}$$

In figure 3c, we demonstrate that the asymptotic approximation of the full arrival data is in close agreement with times generated from a KMC method (described in [35]). In figure 3d, we see that

Table 1. Cumulative count data for arrival for $M = 10^4$ particles at individual receptors for given times. Receptor configuration given in (4.1) with $\varepsilon = 0.1$.

time	c_1	c_2	c_3	$(1/M) \sum_{k=1}^{3} c_k$
$t = 10^0$	580	0	153	0.07
$t = 10^1$	1741	183	973	0.29
$t = 10^3$	2765	929	2070	0.58
$t = \infty$	4192	2194	3614	1.00

$q_k(t) \to \phi_k$ as $t \to \infty$, and in particular we note that this convergence occurs on a long timescale. In figure 3e, we show the instantaneous fluxes into the receptors with the location and height of the peaks indicating the prominence of signal to the receptors. If a cell needs to make a quick ($t \approx 10^0$) decision on the source location, then the $k = 1$ receptor is the primary recipient of signal and gives the best information to make an inference on the source direction. In figure 3f, we show the instantaneous relative fluxes $\bar{\mathcal{J}}_k(t)$ and observe that $\bar{\mathcal{J}}_k(t) \to \bar{\phi}_k$ as $t \to \infty$. The quantities $\bar{\phi}_k$ (see equation (2.8)) reflect the component of the splitting probabilities that are independent of the source location. Therefore, figure 3f provides an estimate of the time ($t \approx 10^2$) beyond which particles attain thermal equilibrium and no longer contain source information.

We now demonstrate source inference in this scenario (parameters (4.1) with $\varepsilon = 0.1$). This configuration of receptors is not representative of a real cell; however, this is an informative test case since $N = 3$ is the minimum required to uniquely locate (triangulate) the source [18]. In this test case, we generated $M = 10^4$ arrival times with the particle approach [35] and took receptor counts at times $t = 10^0$, $t = 10^1$, $t = 10^3$ and $t = \infty$. The count measurements (table 1) demonstrate that short-time data have much richer information on the source direction.

When surveying the counts in table 1, we clearly see the importance of short-time arrival data. For example, by $t = 10^0$, 7% of the particles have been captured yet none have arrived at receptor $k = 2$. This strongly suggests the source is not to the left of the cell and that the signal through receptors $k = 1, 3$ convey richer information on the source location. However, the splitting probabilities, which arise once all particles have been absorbed ($t = \infty$), do not give such a clear conclusion that the source is to the right. Indeed, the smaller deviation in counts across the receptors may diminish the quality of the inference.

To examine further the role of dynamics on source inference, for each time $t = 10^1$, $t = 10^3$ and $t = \infty$ (splitting probabilities), we form 20 MLE estimates $\hat{\mathbf{x}}_{\text{MLE}}$ (figure 4, solid white dots) from $M = 10^4$ arrivals, as defined in (3.2). Simultaneously we plot contours of the exact landscape $\mathcal{L}^*(\mathbf{x}; \mathbf{x}_0, t)$ defined in (3.3), where the shown regions are within $(0.125\%, 0.25\%, 0.5\%, 1.0\%)$ of the minimum of $\mathcal{L}^*$. The contours are shown to correctly envelop the source $\mathbf{x}_0$ while the estimates $\hat{\mathbf{x}}_{\text{MLE}}$ form a cloud surrounding the source $\mathbf{x}_0$. The results in figure 4 demonstrate the robustness of this method under noisy perturbations and corroborate the data in table 1, indicating that the short-time flux yields a tight and clear direction for the source, but a poor estimate on the distance. At the later time $t = 10^3$, and for the splitting probabilities ($t = \infty$), the estimate on the distance is markedly improved.

4.2. Example: circular cell with homogeneous receptor covering

In this example, we consider the scenario of a circular cell of radius $r_{\text{cell}} = 1$ centred at the origin and with $N = 10$ homogeneously spaced receptors of common extent parametrized by

$$\mathbf{x}_k = \left(\cos \frac{2\pi k}{N}, \sin \frac{2\pi k}{N} \right), \quad \ell_k = \varepsilon \ell_c, \quad k = 1, \ldots, N. \tag{4.3}$$

The parameters used are $\varepsilon = \pi/20$, $\ell_c = 1$ and the simulations are initiated with $M = 10^4$ particles at the source $\mathbf{x}_0 = [R, 0]$ for $R > 1$. In particular, we examine the inference landscape $\mathcal{L}^*(\mathbf{x}; \mathbf{x}_0, t)$ and source estimates $\hat{\mathbf{x}}_{\text{MLE}}$ as the source distance R and cumulative signal $C(t) = \int_{\tau=0}^{t} \rho(\tau) \, d\tau$ varies.

In figure 5, we plot contours of the exact landscape $\mathcal{L}^*(\mathbf{x}; \mathbf{x}_0, t)$ and 20 MLE estimates $\hat{\mathbf{x}}_{\text{MLE}}$ over source distances $R = \{2, 5, 10, 20\}$ and absorbed fractions $C(t) = \{2\%, 10\%, 20\%, 100\%\}$. We draw three main conclusions from figure 5. First, the quality of inferred source direction decreases as R increases, which is to be expected when identifying a more distant source. Second, and somewhat
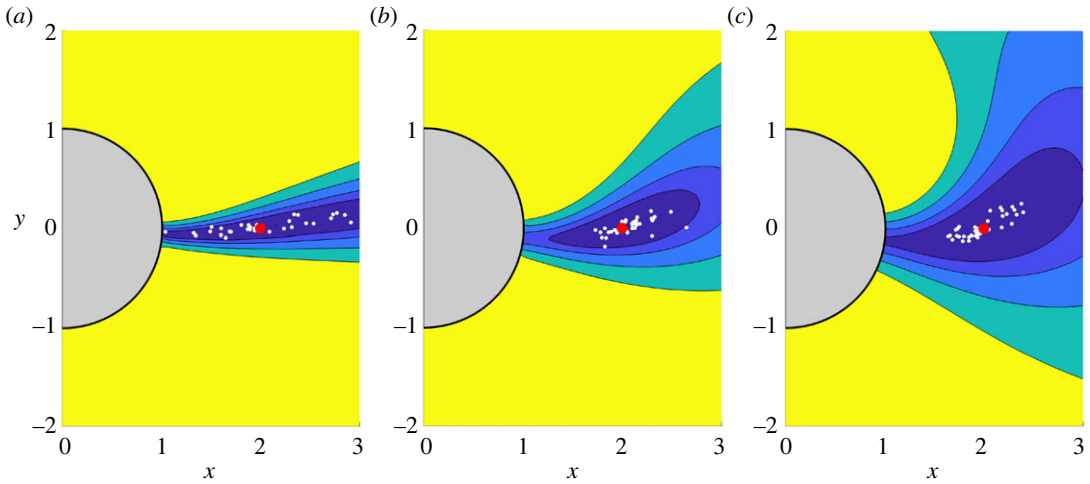
Figure 4. Inference for parameters (4.1) and $\varepsilon = 0.1$. The landscape $\mathcal{L}^*(\mathbf{x}; \mathbf{x}_0, t)$ of (3.3) formed using the relative fluxes (4.2) at $t = 10^1$, $t = 10^3$ and splitting probabilities ($t = \infty$). The source $\mathbf{x}_0 = [2, 0]$ is marked as a red dot and the contours indicate regions where $\mathcal{L}^*(\mathbf{x}; \mathbf{x}_0, t)$ is within $(0.125\%, 0.25\%, 0.5\%, 1.0\%)$ of the estimator $\mathbf{x}_0$. Solid white dots indicate 20 MLE estimates $\mathbf{x}_{\mathrm{MLE}}$ derived from (3.2) using $M = 10^4$ arrival times. (a) $t = 10^1$, (b) $t = 10^3$, (c) $t = \infty$.
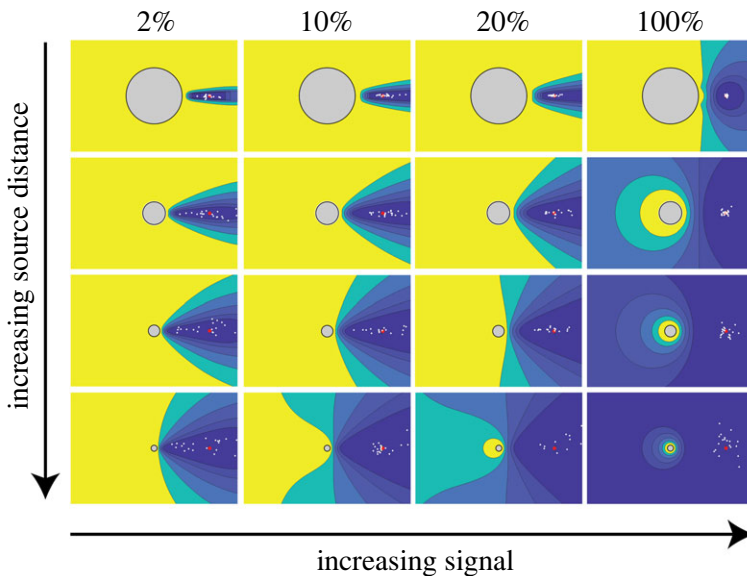

Figure 5. The inference landscape $\mathcal{L}^*(\mathbf{x}; \mathbf{x}_0, t)$ for the example (4.3) with a disc geometry covered by $N = 10$ equally spaced receptors. Horizontal axis indicates the fraction of initial signal captured and vertical axis indicates source distance. Using random samples of size $M = 10^4$ arrivals, we plot 20 $\widehat{\mathbf{x}}_{\mathrm{MLE}}$ estimates (white markers) based on (3.3).

counterintuitively, the precision of the angular estimate on the source direction is reduced as the acquired signal increases. Indeed, at each source distance, the strongest angular signal is acquired from the early arrival data ($C(t) = 2\%$). Third, the effect of noise, shown through the cloud of 20 estimates $\widehat{\mathbf{x}}_{\mathrm{MLE}}$, confirms predictions of the inference landscape $\mathcal{L}^*(\mathbf{x}; \mathbf{x}_0, t)$. Namely that when the acquired signal is low, the directional estimate is accurate. For large acquired signals, the source distance is correctly inferred.

4.3. Example: homogenization and polar momentum

In the above example, MLE inference revealed that early receptor arrivals contained rich information on the source direction. We now explore the efficacy of a simple inference mechanism based on a polar average θ_{pa} of angular receptor positions θ_k weighted by arrival numbers c_k. Specifically, we sort
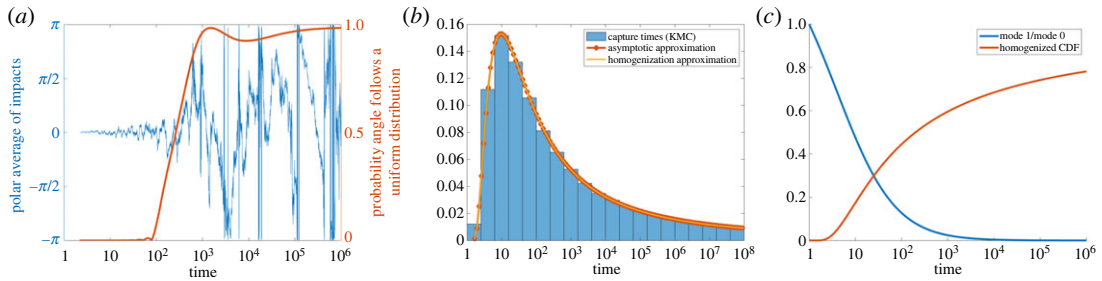
Figure 6. Inferring direction from early arrivals and homogenization. (*a*) Averaged angular receptor input θ_{pa} based on $M_s = 1001$ arrivals (blue) and the *p*-value of Kolmogorov–Smirnov (KS) test compared with uniform cumulative distribution function (CDF) with 5% significance (red). (*b*) Homogenized, KMC and full asymptotics of arrival time distribution in close agreement. (*c*) Ratio of first and second modes of the surface flux (blue) and fraction captured (red). The amplitude of this ratio quantifies the angular information that free particles carry on the source direction.

arrival times and calculate an average θ_{pa} for each batch of M_s arrivals

$$\theta_{\mathrm{pa}} = \frac{1}{M_s}\sum_{k=1}^{N} c_k \theta_k, \qquad \sum_{k=1}^{N} c_k = M_s.$$

In figure 6, we show results for $N = 100$ homogeneously spaced receptors occupying half the cellular surface for $M_s = 1001$. The KMC simulations are initiated by $M = 10^5$ particles at location $\mathbf{x}_0 = (5, 0)$ with diffusivity $D = 1$. Figure 6*a* shows that a simple average of receptor input gives an excellent estimate of source direction for short times ($t \lesssim 10^3$). At larger times ($t \gtrsim 10^3$), the directional information in the signal vanishes and the polar average becomes uniform $\mathcal{U}[-\pi, \pi]$, as shown by the *p*-value of a Kolmogorov–Smirnov (KS) test with 5% significance. To explain this sharp transition, we use the homogenized solution and calculate from (2.35) that $\kappa = 206.98$. We show the arrival time distribution (figure 6*b*) and the ratio of the first to zeroth modes (figure 6*c*) of the homogenized surface flux $\mathcal{L}^{-1}(\chi_1(s))/\mathcal{L}^{-1}(\chi_0(s))$ derived in (B 10). The transition coincides with the amplitude of this ratio diminishing. This corresponds to the surface flux becoming more radially symmetric so that the remaining free particles carry no directional information on the source. The associated homogenized cumulative distribution function (CDF) for this example predicts that at the transition time ($t \approx 10^3$), the remaining approximately 60% of free particles have no angular information corresponding to their initial position (figure 6*c*).

4.4. Example: extreme arrivals to an all-absorbing cell

In the preceding examples, we have observed that early arrivals give significant directional information on the source. To establish a theoretical bound of the accuracy on source detection based the first of M independent arrivals, we consider the time and impact distribution to a homogenized circular cell of radius $r_{\mathrm{cell}} = 1$. The arrival times are $\mathcal{T}_M = \{t_1, t_2, \ldots, t_M\}$ with corresponding arrival angles $\Theta_M = \{\theta_1, \theta_2, \ldots, \theta_M\}$. We remark that the arrival times $\mathcal{T}_M$ and associated angles Θ_M are not independent and in general longer times give rise to uniform angles, while at shorter times the angular distribution is centred on the source direction. The random variable $t_{\mathrm{a}} = \min \mathcal{T}_M$ is known as the *extreme arrival time* and θ_{a} is the polar coordinate of the associated arrival location. The distribution of t_{a} for $M \gg 1$ was recently found (see [38], Theorem 1) to satisfy

$$\frac{t_{\mathrm{a}} - b_M}{a_M} \to X, \quad \text{as } M \to \infty, \tag{4.4}$$

where X follows the Gumbel distribution $\mathbb{P}(X > x) = \exp(-\mathrm{e}^x)$. The quantities a_M, b_M are determined in terms of the short-time asymptotics of the probability $P(t) = \mathbb{P}(t_1 > t)$ of a single walker. For a given q, $A \neq 0$ and $B > 0$, we have that

$$1 - P(t) \sim A t^q \, \mathrm{e}^{-B/t}, \quad \text{as } t \to 0^+ \tag{4.5a}$$

and

$$a_M = \frac{b_M}{q(1 + W_M)}, \quad b_M = \frac{B}{qW_M}, \quad W_M = W_*\left(\frac{B}{q}(AM)^{1/q}\right), \tag{4.5b}$$

where $W_*(z)$ is the principal branch of the LambertW function, defined as the inverse function of $f(z) = z\,e^z$. The mean and variance of the Gumbel distribution are

$$\mathbb{E}[t_a] = b_M - \gamma_e a_M \quad \text{and} \quad \text{Var}[t_a] = \frac{\pi^2}{6}a_M^2, \tag{4.6}$$

where $\gamma_e \approx 0.5772$ is the Euler–Mascheroni constant. We are able to identify in the homogenized scenario that the relevant parameters (B 13) are

$$q = \frac{3}{2}, \quad A = \frac{\sqrt{D}}{\sqrt{\pi R}}\frac{4\kappa}{(R-1)^2}, \quad B = \frac{(R-1)^2}{4D}. \tag{4.7}$$

In terms of the expectation, we have that as $M \to \infty$

$$\mathbb{E}[t_a] \sim \frac{(R-1)^2}{6DW_M}\left[1 - \frac{2\gamma_e}{3(1+W_M)}\right]. \tag{4.8}$$

For the arrival time t_a, the associated arrival location θ_a in polar coordinates is calculated as

$$\mathbb{P}[\theta_a = \eta] = \int_{\tau=0}^{\infty} \mathbb{P}[\theta = \eta|t = \tau]\,\mathbb{P}[t_a = \tau]\,d\tau \tag{4.9}$$

$$= \frac{1}{a_M}\int_{\tau=0}^{\infty} \mathbb{P}[\theta = \eta|t = \tau]\,e^{-z-e^z}\,d\tau, \quad z = \left(\frac{\tau - b_M}{a_M}\right). \tag{4.10}$$

To approximate this integral, consider that $-z - e^z$ has a critical point at $z = 0$ ($t = b_M$) and so

$$e^{-z-e^z} \approx \exp\left[-1 - \frac{(t-b_M)^2}{2a_M^2}\right], \quad (t - b_M)^2 \ll 1.$$

Therefore, we see that applying Laplace's method yields

$$\mathbb{P}[\theta_a = \eta] \approx e^{-1}\int_{\tau=0}^{\infty} \mathbb{P}[\theta = \eta|t = \tau]\frac{1}{a_M}\exp\left[-\frac{(\tau-b_M)^2}{2a_M^2}\right]\,d\tau$$

$$\approx \sqrt{2\pi}e^{-1}\,\mathbb{P}[\theta = \eta|t = b_M]. \tag{4.11}$$

We note that $t = b_M$ is the mode of the Gumbel distribution and the factor $\sqrt{2\pi}e^{-1} \approx 0.922$ is an error induced by the Laplace approximation that we normalize to unity. For $b_M \ll 1$, the result (2.39) indicates that $\mathbb{P}[\theta = \eta|t = b_M] \sim \mathcal{N}(\theta_0, 2Db_M/R)$. After algebra, we conclude that as $M \to \infty$, the arrival angle is distributed $\theta_a \sim \mathcal{N}(\theta_0, \sigma_{\theta_a}^2)$ with variance $\sigma_{\theta_a}^2$ given by

$$\sigma_{\theta_a}^2(M, R) = \frac{g(R)}{W_M}, \quad g(R) = \frac{(R-1)^2}{3R}, \quad W_M = W_*\left[\left(\frac{2\kappa^2 M^2}{9\pi D^2}g(R)\right)^{1/3}\right].$$

We remark that $W_*(z) \sim \log z$ as $z \to \infty$ giving the leading order behaviour as $M \to \infty$

$$\sigma_{\theta_a}^2(M, R) \propto \frac{R(1 - (1/R))^2}{\log M}. \tag{4.12}$$

The relationship (4.12) implies that provided the signal strength M is large enough and the source is not too distant, the first arrival yields the source direction with reasonable accuracy.

As a demonstration of this theory, we consider the scenario of a cell of radius $r_{cell} = 1$ centred at the origin with $N = 100$ homogeneously spaced receptors occupying 10% of the surface. We calculate t_a from (4.8) and the associated arrival angle θ_a. We plot in figure 7 comparisons between the extreme value statistics and numerical data based on 1000 KMC simulations each with $M = 10^6$ particles. We observe in figure 7a that the distribution of t_a is well predicted by the extreme value theory over six orders of magnitude. The distribution of angular arrivals θ_a is also very well predicted by (4.12) as shown in figure 7b. Remarkably, this result shows that a cell can make an informed decision on the source direction based on just a single arriving signalling molecule, provided the source distance R is not too large.
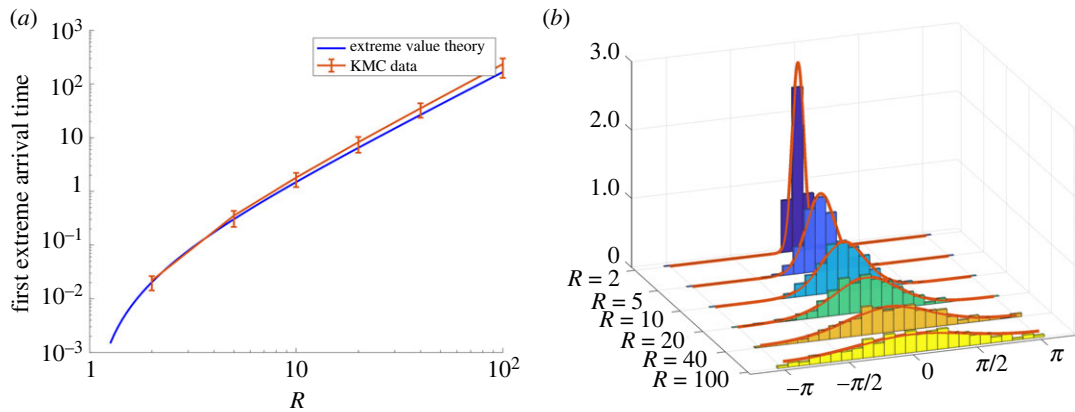
Figure 7. The distribution of extreme arrival times t_a and their angular distribution with $M = 10^6$ particles averaged over 1000 simulations. (*a*) The first arrival time t_a against R. (*b*) Comparison of angular distributions of the first arrival from KMC and theory (solid red) for various R.

We now provide a *rough* comparison between the timescales predicted by extreme statistics (4.8) and those observed in experiments. We consider an example of directional sensing in neutrophils where a cellular reaction was observed after approximately 5 s when exposed to a point source of chemoattractant (10 µM, fMLP) placed by pipette [58]. This response combines the time to acquire receptor input and to complete downstream signalling dynamics. To approximate the former of these two timescales, we assume $N \approx 10^4$ fMLP receptors [59] of individual radius roughly $r_a = 5$ nm [60], which lies in the validity of the homogenization limit (2.35). If we assume a volume 1 µl is released from a micropipette, this yields an effective particle number $M \approx 10^{12}$. The diffusivity of the chemoattractant fMLP has been estimated at $D = 1.2 \times 10^{-6}$ cm^2 s^{-1} [61]. If we consider cell radii in the range $r_{cell} = 5$–10 µm and sources in the range $r_{source} = 5$–10 r_{cell}, the first extreme arrival time in light of these parameters is $\mathbb{E}[t_a] \approx 0.05$–1 s. The predictions of extreme statistics are of roughly the same order of magnitude as those observed experimentally and provide a minimum time for a cell to respond to a diffusive signal.

5. Discussion

In this paper, we have explored source inference from the dynamics of the diffusive fluxes to localized surface receptors. A key ingredient in our analysis is the application of a new hybrid asymptotic-numerical method that allows for the rapid and accurate determination of the time-dependent solution to an exterior parabolic problem. These quantities give a more detailed understanding of cellular response to external signals than previously available through static quantities (e.g. the splitting probabilities). The full arrival statistics describe both the equilibration timescale and the short-time dynamics of the signal to the cell. As an application of these newly obtained dynamic quantities, we explored their use in source inference.

This work leads to several conjectures that may have biological implications. First, we observe that the equilibration timescale is long and therefore steady-state quantities may not be useful for understanding cellular responses, particularly in dynamic environments. Second, we observe that the earliest arrivals to the surface receptors contain the most directional information. Therefore, a cell can make a quick and accurate directional decision, at the cost of accuracy in source distance, by heavily weighting the earliest signal it receives.

In the extreme scenario where the cell chooses a direction based on just one arrival to its membrane, we find that the accuracy is surprisingly good provided the source distance is not large. An important characteristic of simplistic directional inference methods is that they make minimal biological assumptions regarding cellular computing abilities, memory of previous receptor engagements, knowledge of cellular geometry and receptor configurations. This work suggests that a cell can take simple averages over a small number of signalling receptors to accurately infer the location of nearby signalling sources.

Appendix A. Inner solution at a receptor

A key ingredient in the asymptotic analysis of both the static splitting probabilities (1.1) and the Laplace transform problem (2.12), is knowledge of the solution to a rescaled version of (1.1) in the $\mathcal{O}(\varepsilon)$ neighbourhood of each receptor. This inner solution is a half-plane problem where the curvature of the cell is negligible, the receptor is replaced by an absorbing segment, and the response to the externally varying probability density is quasi-static. In the unrescaled outer problem, the receptor is replaced by a δ-function and the response can be analysed via a surface Green's function.

In an $\mathcal{O}(\varepsilon)$ neighbourhood of the jth receptor centred at $\mathbf{x}_j = (x_j, y_j)$, the solution is described in terms of a local arc-length coordinate system (η, σ) where η represents the distance from $\mathbf{x} \in \mathbb{R}^2 \setminus \Omega$ to $\partial\Omega$ and σ denotes arc-length along $\partial\Omega$. In this system, the Laplacian becomes

$$\Delta := \frac{\partial^2}{\partial\eta^2} - \frac{\bar{\kappa}}{1 - \bar{\kappa}\eta}\frac{\partial}{\partial\eta} + \frac{1}{1 - \bar{\kappa}\eta}\frac{\partial}{\partial\sigma}\left(\frac{1}{1 - \bar{\kappa}\eta}\frac{\partial}{\partial\sigma}\right). \tag{A 1}$$

Here, $\bar{\kappa} = \bar{\kappa}(\sigma)$ is the curvature along $\partial\Omega$. In the arc-length coordinate system, the receptor centre becomes $(\eta, \sigma) = (0, \sigma_j)$. Rescaling in the receptor neighbourhood with $\hat{\eta} = \eta/\varepsilon$ and $\hat{\sigma} = (\sigma - \sigma_j)/\varepsilon$, the Laplacian becomes $\Delta \to \varepsilon^{-2}(\partial^2_{\hat{\eta}\hat{\eta}} + \partial^2_{\hat{\sigma}\hat{\sigma}}) + \mathcal{O}(\varepsilon^{-1})$ and we have the half-plane problem

$$\frac{\partial^2 v_c}{\partial\hat{\eta}^2} + \frac{\partial^2 v_c}{\partial\hat{\sigma}^2} = 0, \quad \hat{\sigma} \in (-\infty, \infty), \quad \hat{\eta} > 0; \tag{A 2a}$$

$$v_c = 0, \quad |\hat{\sigma}| < \ell_j/2, \quad \hat{\eta} = 0; \quad \partial_{\hat{\eta}} v_c = 0, \quad |\hat{\sigma}| > \frac{\ell_j}{2}, \quad \hat{\eta} = 0 \tag{A 2b}$$

and

$$v_c = \log[\hat{\eta}^2 + \hat{\sigma}^2]^{1/2} - \log d_j + \cdots, \quad \text{as } \hat{\eta}^2 + \hat{\sigma}^2 \to \infty, \quad d_j = \frac{\ell_j}{4}. \tag{A 2c}$$

The solution of (A 2) can be obtained by use of the elliptical coordinate system [55] and is used to construct solutions of (1.1) and (2.12). We remark that when applying this boundary layer analysis to the Helmholtz problem (2.11), we assume that $s\varepsilon^2 \ll 1$ and consequently cannot expect a valid expansion near the receptors for arbitrarily short times. In §2.4, we consider separately the short-time surface fluxes in the limit $t \to 0^+$.

Appendix B. Green's functions

In this appendix, we tabulate the various Green's functions for Laplace's equation and the Helmholtz equation that arise from the Laplace transform of the heat equation.

B.1. Half-plane

In the case of the half-plane ($\Omega := \{\mathbf{x} = (x, y) \in \mathbb{R}^2 \mid y > 0\}$) with a Neumann boundary condition, we have the following exact Green's functions satisfying Laplace's equation (2.4) and the Helmholtz equation (2.15), respectively,

$$G_s(\mathbf{x}; \boldsymbol{\xi}) = \frac{-1}{2\pi}\begin{cases} \log|\mathbf{x} - \boldsymbol{\xi}| + \log|\mathbf{x} - \boldsymbol{\xi}'|, & \xi_2 > 0; \\ 2\log|\mathbf{x} - \boldsymbol{\xi}|, & \xi_2 = 0 \end{cases} \tag{B 1a}$$

and

$$G_h(\mathbf{x}; \boldsymbol{\xi}, s) = \frac{1}{2\pi D}\begin{cases} K_0(\alpha|\mathbf{x} - \boldsymbol{\xi}|) + K_0(\alpha|\mathbf{x} - \boldsymbol{\xi}'|), & \xi_2 > 0; \\ 2K_0(\alpha|\mathbf{x} - \boldsymbol{\xi}|), & \xi_2 = 0 \end{cases}, \tag{B 1b}$$

where $\boldsymbol{\xi} = (\xi_1, \xi_2)$ is the location of the source in the bulk, $\boldsymbol{\xi}' = (\xi_1, -\xi_2)$ is the source's image in the half-plane, $K_0(z)$ is a modified Bessel function, and $\alpha = \sqrt{s/D}$.

B.2. Unit disc

In the case of a unit disc ($\Omega := \{\mathbf{x} = (x, y) \in \mathbb{R}^2 \mid x^2 + y^2 < 1\}$), we first solve for Green's function G_s for the Laplacian (2.4). In terms of polar variables (r, θ) and $\boldsymbol{\xi} = e^{i\theta_0}$, the problem to be solved is

$$\frac{\partial^2 G_s}{\partial r^2} + \frac{1}{r}\frac{\partial G_s}{\partial r} + \frac{1}{r^2}\frac{\partial^2 G_s}{\partial \theta^2} = 0, \quad r > 1, \quad \theta \in (0, 2\pi); \tag{B 2a}$$

$$G_s(r, \theta; \theta_0) = G_s(r, \theta + 2\pi, \theta_0), \quad r > 1, \quad \theta \in (0, 2\pi) \tag{B 2b}$$

and

$$-\frac{\partial G_s}{\partial r} = \delta(\theta - \theta_0), \quad r = 1, \quad \theta \in (0, 2\pi). \tag{B 2c}$$

The separable solution of (B 2) can be expressed in the cosine series

$$G_s(r, \theta; \theta_0) = \frac{-1}{2\pi}\log r + \frac{1}{\pi}\sum_{n=1}^{\infty}\frac{\cos n(\theta - \theta_0)}{nr^n}.$$

The series can be summed directly by defining $\mathbf{x} = re^{i\theta}$ and specifying that

$$\sum_{n=1}^{\infty}\frac{\cos n(\theta - \theta_0)}{nr^n} = \mathrm{Re}\left[\sum_{n=1}^{\infty}\frac{1}{n}\left(\frac{\mathbf{x}}{|\mathbf{x}|^2\boldsymbol{\xi}}\right)^n\right] = -\log\left|1 - \frac{\mathbf{x}}{|\mathbf{x}|^2\boldsymbol{\xi}}\right| = -\frac{1}{2}\log\left|\frac{\mathbf{x} - \boldsymbol{\xi}}{\mathbf{x}}\right|^2. \tag{B 3}$$

After rearranging, we obtain that

$$G_s(\mathbf{x}; \boldsymbol{\xi}) = -\frac{1}{\pi}\log|\mathbf{x} - \boldsymbol{\xi}| + R_s(\mathbf{x}; \boldsymbol{\xi}) \quad \text{and} \quad R_s(\mathbf{x}; \boldsymbol{\xi}) = \frac{1}{2\pi}\log|\mathbf{x}|.$$

For Helmholtz Green's function exterior to the disc with source $\boldsymbol{\xi} = Re^{i\theta_0}$, we examine the form of the series for $R = 1$ and $R > 1$ separately.

B.2.1. Unit disc with a source on the surface

In this scenario, the surface Helmholtz Green's function satisfies

$$D\left[\frac{\partial^2 G_h}{\partial r^2} + \frac{1}{r}\frac{\partial G_h}{\partial r} + \frac{1}{r^2}\frac{\partial^2 G_h}{\partial \theta^2}\right] - sG_h = 0, \quad r > 1, \quad \theta \in (0, 2\pi); \tag{B 4a}$$

$$G_h(r, \theta; \theta_0) = G_h(r, \theta + 2\pi, \theta_0), \quad r > 1, \quad \theta \in (0, 2\pi) \tag{B 4b}$$

and

$$-D\frac{\partial G_h}{\partial r} = \delta(\theta - \theta_0), \quad r = 1, \quad \theta \in (0, 2\pi). \tag{B 4c}$$

The appropriate separable solution is then the Bessel cosine series

$$G_h(r, \theta; \theta_0) = \frac{-1}{2\pi D}\frac{K_0(\alpha r)}{\alpha K_0'(\alpha)} - \frac{1}{\pi D}\sum_{n=1}^{\infty}\frac{K_n(\alpha r)}{\alpha K_n'(\alpha)}\cos n(\theta - \theta_0).$$

To isolate the singular and regular parts, we add and subtract a term $(1/\pi D)\log|\mathbf{x} - \boldsymbol{\xi}|)$ and replace one with the identity (B 3). This reveals that for $\mathbf{x} = re^{i\theta}$ and $\boldsymbol{\xi} = e^{i\theta_0}$

$$G_h(\mathbf{x}; \boldsymbol{\xi}) = -\frac{1}{\pi D}\log|\mathbf{x} - \boldsymbol{\xi}| + R_h(\mathbf{x}; \boldsymbol{\xi}) \tag{B 5a}$$

and

$$R_h(\mathbf{x}; \boldsymbol{\xi}) = \frac{1}{\pi D}\left(\log r - \frac{1}{2}\frac{K_0(\alpha r)}{\alpha K_0'(\alpha)} - \sum_{n=1}^{\infty}\left[\frac{K_n(\alpha r)}{\alpha K_n'(\alpha)} + \frac{1}{nr^n}\right]\cos n(\theta - \theta_0)\right). \tag{B 5b}$$

Using the well-known large order asymptotics (https://dlmf.nist.gov/10.41) of $K_n(z) \sim \sqrt{\pi/2n}[ez/2n]^{-n}$ as $n \to \infty$, we observe that

$$\frac{K_n(\alpha r)}{\alpha K_n'(\alpha)} \sim \frac{-1}{nr^n}, \quad n \to \infty,$$

and therefore the series in (B 5b) is convergent, including as $r \to 1$.

B.2.2. Unit disc with a source in the bulk

Here, the Helmholtz Green's function satisfies

$$D\left[\frac{\partial^2 G_h}{\partial r^2} + \frac{1}{r}\frac{\partial G_h}{\partial r} + \frac{1}{r^2}\frac{\partial^2 G_h}{\partial \theta^2}\right] - sG_h = -\frac{1}{r}\delta(r-R)\delta(\theta-\theta_0), \quad r > 1, \quad \theta \in (0, 2\pi); \quad \text{(B 6a)}$$

$$G_h(r, \theta; \theta_0) = G_h(r, \theta + 2\pi, \theta_0), \quad r > 1, \quad \theta \in (0, 2\pi) \quad \text{(B 6b)}$$

and

$$\frac{\partial G_h}{\partial r} = 0, \quad r = 1, \quad \theta \in (0, 2\pi). \quad \text{(B 6c)}$$

The separable solution which is continuous and satisfies $\partial_r G_h = 0$ on $r = 1$ is given by

$$G_h = \begin{cases} \sum_{n=0}^{\infty} A_n \left[I_n(\alpha r)K_n'(\alpha) - I_n'(\alpha)K_n(\alpha r)\right]\frac{K_n(\alpha R)}{K_n'(\alpha)}\cos n(\theta - \theta_0), & 1 < r < R; \\ \sum_{n=0}^{\infty} A_n \left[I_n(\alpha R)K_n'(\alpha) - I_n'(\alpha)K_n(\alpha R)\right]\frac{K_n(\alpha r)}{K_n'(\alpha)}\cos n(\theta - \theta_0), & r > R. \end{cases} \quad \text{(B 7)}$$

Applying the jump condition and the orthogonality of the functions $\{\cos m(\theta - \theta_0)\}_{m=0}^{\infty}$ yields

$$D\lim_{\delta \to 0}\int_{r=R-\delta}^{r=R+\delta}\int_{\theta=0}^{2\pi}\cos m(\theta - \theta_0)\frac{1}{r}\frac{\partial}{\partial r}\left(r\frac{\partial G_h}{\partial r}\right)r\,dr\,d\theta = -1,$$

which fixes the constants

$$A_0 = \frac{1}{2\pi D}, \quad A_n = \frac{1}{\pi D}, \quad n \geq 1.$$

Finally, our interest is in $G_h|_{r=1}$, which is written as the series

$$G_h|_{r=1}(\theta; R, \theta_0) = -\frac{1}{2\pi D}\frac{K_0(\alpha R)}{\alpha K_0'(\alpha)} - \frac{1}{\pi D}\sum_{n=1}^{\infty}\frac{K_n(\alpha R)}{\alpha K_n'(\alpha)}\cos n(\theta - \theta_0). \quad \text{(B 8)}$$

In the above calculations, we have used the Wronskian Identity $I_n'(z)K_n(z) - I_n(z)K_n'(z) = z^{-1}$. We apply (B 8) only in the situation $|\xi| = R > 1$ such that the series converges rapidly.

B.2.3. Unit disc with a homogenized surface (Robin condition)

We are interested in the solution $p_h(r, \theta, t; R)$ of the heat equation with Robin condition, defined by (2.20). We consider the problem exterior to the disc of radius $r_{cell} = 1$ with a source at $R(\cos\theta_0, \sin\theta_0)$. We apply the Laplace transform $G_h(r, \theta; s) = \int_{t=0}^{\infty} p_h(r, \theta, t)e^{st}\,dt$, and find that G_h solves the Helmholtz Green's function

$$D\left[\frac{\partial^2 G_h}{\partial r^2} + \frac{1}{r}\frac{\partial G_h}{\partial r} + \frac{1}{r^2}\frac{\partial^2 G_h}{\partial \theta^2}\right] - sG_h = -\frac{1}{r}\delta(r-R)\delta(\theta-\theta_0), \quad r > 1, \quad \theta \in (0, 2\pi); \quad \text{(B 9a)}$$

$$G_h(r, \theta; \theta_0) = G_h(r, \theta + 2\pi, \theta_0), \quad r > 1, \quad \theta \in (0, 2\pi) \quad \text{(B 9b)}$$

and

$$D\frac{\partial G_h}{\partial r} = \kappa G_h, \quad r = 1, \quad \theta \in (0, 2\pi). \quad \text{(B 9c)}$$

Similar to the Neumann case above, we obtain a continuous separable solution satisfying a jump condition at $r = R$ and the Robin condition at $r = 1$. Our interest is in the surface flux given by

$$D\partial_r G_h|_{r=1} = \frac{1}{2\pi}\chi_0(\alpha) + \frac{1}{\pi}\sum_{n=1}^{\infty}\chi_n(\alpha)\cos n(\theta - \theta_0) \quad \text{and} \quad \chi_n(\alpha) = \frac{K_n(\alpha R)}{K_n(\alpha) - D\kappa^{-1}\alpha K_n'(\alpha)}, \quad \text{(B 10)}$$

where $zK_n'(z) = n\,K_n(z) - zK_{n+1}(z)$ and $\alpha = \sqrt{\frac{s}{D}}$. The total flux through the disc is

$$\widehat{\mathcal{J}}(s) = \int_0^{2\pi} D\partial_r G_h|_{r=1}\,d\theta = \chi_0(\alpha) = \frac{K_0(\alpha R)}{K_0(\alpha) - D\kappa^{-1}\alpha K_0'(\alpha)}. \quad \text{(B 11)}$$

One of our goals is to find the limiting behaviour of the survival probability $P(t) = \int_{r=1}^{\infty}\int_{\theta=0}^{2\pi} p_h(r, \theta, t)r\,d\theta\,dr$ as $t \to 0$. Here again $p_h(r, \theta, t)$ solves (2.20). The relationship $P'(t) = -\mathcal{J}(t)$ connects the survival probability with surface flux and therefore in transform space $\widehat{\mathcal{J}}(s) = 1 - s\widehat{P}(s)$. The limit as $t \to 0^+$ corresponds to $s \to \infty$ in transform space yielding

$$\widehat{P}(s) = \frac{1}{s} - \frac{\kappa}{s^{3/2}\sqrt{RD}}e^{-\sqrt{s}[(R-1)/\sqrt{D}]}, \quad s \to \infty \quad \text{(B 12a)}$$
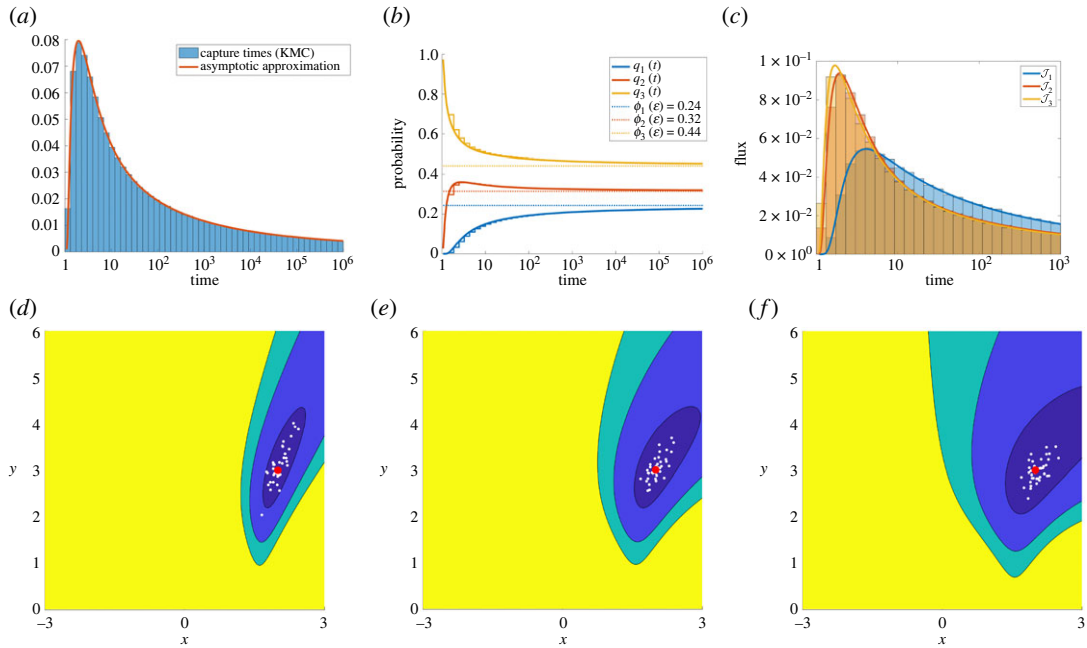
Figure 8. Flux dynamics and source recovery for the half-plane example (D 1). (*a*) The full distribution of first passage times from (4.2) and $M = 10^5$ arrival times obtained with kinetic Monte Carlo (KMC). (*b*) Time-dependent signals (4.2) with asymptotic splitting probabilities $\{\phi_1, \phi_2, \phi_3\}$ for parameters (D 1) and $\varepsilon = 0.1$. (*c*) Dynamics of individual receptor fluxes. (*d*–*f*) Inference landscape $\mathcal{L}(\mathbf{x}; t)$ for the half-plane example with parameters specified in (D 1). Inference performed using cumulative receptor signal at times $t = 10^1$ (*d*), $t = 10^3$ (*e*) and $t = \infty$ (*f*).

and

$$P(t) = 1 - \frac{4\kappa}{\sqrt{\pi R}} \frac{\sqrt{D}}{(R-1)^2} t^{3/2} e^{(-(R-1)^2)/4tD}, \quad t \to 0^+. \tag{B 12b}$$

The limiting form identified in (B 12*b*) is consistent with the short-time asymptotics (2.39*b*), after evaluating $\int_0^t \mathcal{M}_0(\tau)\,d\tau$ as $t \to 0^+$. From (B 12*b*), we identify the coefficients $P(t) = 1 - A\,t^q\,e^{-(B/t)}$ as

$$q = \frac{3}{2}, \quad A = \frac{\sqrt{D}}{\sqrt{\pi R}} \frac{4\kappa}{(R-1)^2} \quad \text{and} \quad B = \frac{(R-1)^2}{4D}. \tag{B 13}$$

Appendix C. Least-squared solution of splitting problem

Here, we describe a numerical technique for the solution of (1.1) exterior to the unit disc. In polar coordinates (r, θ), the solution (subscript of distinguished receptor omitted) has separable form

$$\phi(r, \theta) = \frac{a_0}{2} + \sum_{n=1}^{\infty} r^{-n}(a_n \cos n\theta + b_n \sin n\theta). \tag{C 1a}$$

The coefficients are found by applying the Neumann and Dirichlet conditions to arrive at the following dual trigonometric series:

$$\frac{a_0}{2} + \sum_{n=1}^{\infty}(a_n \cos n\theta + b_n \sin n\theta) = \begin{cases} 1 & \text{distinguished receptor,} \\ 0 & \text{other receptors;} \end{cases} \tag{C 1b}$$

and

$$\sum_{n=1}^{\infty} n(a_n \cos n\theta + b_n \sin n\theta) = 0, \quad \text{reflecting portion.} \tag{C 1c}$$

Progress can be made on analytical solutions of this dual series [56]; however, in the present scenario, it is more convenient to access the solution numerically. The series (C 1*a*) is truncated at a finite number of

modes M and a linear system for the $(2M+1)$ coefficients formed by introducing a grid of θ values. At each value of θ, the entries of the system are filled according to the conditions (C 1b) and (C 1c), resulting in an overdetermined system that is solved by least-squared solutions. We find (figure 3) that this solution approach is robust and accurate for moderately small receptor extents; however, the number of modes M is prohibitive for very small receptors. See [56,62,63] for more details on this solution procedure.

Appendix D. Half-plane with three receptors

As a supplemental example, we consider a three-receptor scenario in the upper half-plane. In this geometry, the cell Ω does not have a finite area so it is necessarily a simplification of the biological setting. However, it can be useful [18] to examine both the asymptotic formulations and the source inference approach. In this context, the specific parameters used in this example are

$$\ell = \varepsilon\left[\frac{1}{2},\ 1,\ 2\right], \quad \mathbf{x}_1 = [-3, 0], \ \mathbf{x}_2 = [0, 0], \ \mathbf{x}_3 = [3, 0], \ D = 4, \ \varepsilon = 0.1, \ \mathbf{x}_0 = [2, 3]. \qquad (D\,1)$$

In figure 8, we show that the asymptotic formulations of both the splitting probabilities and the arrival time distribution agree very well with Monte Carlo data. As with the disc case, the convergence $q_k(t) \to \phi_k$ as $t \to \infty$ is observed on a long timescale.

In the upper half-plane geometry, we do not have a 'shielding effect' in which the geometry itself delays the arrival of particles to the distant receptors. We observe in figure 8a that the short-time data provide only rough directional information and reflecting that the source is to the right of the origin. At moderate time $t = 10^3$, we observe in figure 8e a stronger angular signal (with respect to the origin) while the splitting probabilities show recovery of source distance and angle (figure 8f).

References

1. Levchenko A, Iglesias PA. 2002 Models of eukaryotic gradient sensing: application to chemotaxis of amoebae and neutrophils. *Biophys. J.* **82**, 50–63. (doi:10.1016/S0006-3495(02)75373-3)

2. Varennes J, Moon H, Saha S, Mugler A, Han B. 2019 Physical constraints on accuracy and persistence during breast cancer cell chemotaxis. *PLoS Comput. Biol.* **15**, 1–20. (doi:10.1371/journal.pcbi.1006961)

3. Kim H, Mori Y, Plotkin JB. 2022 Optimality of intercellular signaling: direct transport versus diffusion. *Phys. Rev. E* **106**, 054411. (doi:10.1103/PhysRevE.106.054411)

4. Goodhill GJ. 2016 Can molecular gradients wire the brain? *Trends Neurosci.* **39**, 202–211. (doi:10.1016/j.tins.2016.01.009)

5. Ismael A et al. 2016 Gβ promotes pheromone receptor polarization and yeast chemotropism by inhibiting receptor phosphorylation. *Sci. Signal.* **9**, 1–17. (doi:10.1126/scisignal.aad4376)

6. Henderson NT, Pablo M, Ghose D, Clark-Cotton MR, Zyla TR, Nolen J, Elston TC, Lew DJ. 2019 Ratiometric GPCR signaling enables directional sensing in yeast. *PLoS Biol.* **17**, 1–35. (doi:10.1371/journal.pbio.3000484)

7. Park S, Kim H, Wang Y, Eom DS, Allard J. 2022 Zebrafish airinemes optimize their shape between ballistic and diffusive search. *eLife* **11**, e75690. (doi:10.7554/eLife.75690)

8. Song L, Nadkarni SM, Bödeker HU, Beta C, Bae A, Franck C, Rappel WJ, Loomis WF, Bodenschatz E. 2006 *Dictyostelium discoideum* chemotaxis:

threshold for directed motion. *Eur. J. Cell Biol.* **85**, 981–989. (doi:10.1016/j.ejcb.2006.01.012)

9. Van Haastert PJ, Postmay M. 2007 Biased random walk by stochastic fluctuations of chemoattractant-receptor interactions at the lower limit of detection. *Biophys. J.* **93**, 1787–1796. (doi:10.1529/biophysj.107.104356)

10. Tostevin F, Ten Wolde PR, Howard M. 2007 Fundamental limits to position determination by concentration gradients. *PLoS Comput. Biol.* **3**, 763–771. (doi:10.1371/journal.pcbi.0030078)

11. Rappel WJ, Levine H. 2008 Receptor noise and directional sensing in eukaryotic chemotaxis. *Phys. Rev. Lett.* **100**, 6–9. (doi:10.1103/PhysRevLett.100.228101)

12. Endres RG, Wingreen NS. 2008 Accuracy of direct gradient sensing by single cells. *Proc. Natl Acad. Sci. USA* **105**, 15 749–15 754. (doi:10.1073/pnas.0804688105)

13. Endres RG, Wingreen NS. 2009 Accuracy of direct gradient sensing by cell-surface receptors. *Prog. Biophys. Mol. Biol.* **100**, 33–39. (doi:10.1016/j.pbiomolbio.2009.06.002)

14. Aquino G, Tweedy L, Heinrich D, Endres RG. 2014 Memory improves precision of cell sensing in fluctuating environments. *Sci. Rep.* **4**, 1–9. (doi:10.1038/srep05688)

15. Strünker T, Alvarez L, Kaupp UB. 2015 At the physical limit — chemosensation in sperm. *Curr. Opin. Neurobiol.* **34**, 110–116. (doi:10.1016/j.conb.2015.02.007)

16. Lakhani V, Elston TC. 2017 Testing the limits of gradient sensing. *PLoS Comput. Biol.* **13**, 1–30. (doi:10.1371/journal.pcbi.1005386)

17. Kurella V, Tzou JC, Coombs D, Ward MJ. 2015 Asymptotic analysis of first passage time problems inspired by ecology. *Bull. Math. Biol.* **77**, 83–125. (doi:10.1007/s11538-014-0053-5)

18. Dobramysl U, Holcman D. 2018 Mixed analytical-stochastic simulation method for the recovery of a Brownian gradient source from probability fluxes to small windows. *J. Comput. Phys.* **355**, 22–36. (doi:10.1016/j.jcp.2017.10.058)

19. Dobramysl U, Holcman D. 2021 Reconstructing a point source from diffusion fluxes to narrow windows in three dimensions. *Proc. R. Soc. A* **477**, 20210271. (doi:10.1098/rspa.2021.0271)

20. Perelson AS, Weisbuch G. 1997 Immunology for physicists. *Rev. Mod. Phys.* **69**, 1219–1268. (doi:10.1103/RevModPhys.69.1219)

21. Lawley SD, Lindsay AE, Miles CE. 2020 Receptor organization determines the limits of single-cell source location detection. *Phys. Rev. Lett.* **125**, 018102. (doi:10.1103/PhysRevLett.125.018102)

22. Redner S. 2001 *A guide to first-passage processes*. Cambridge, UK: Cambridge University Press.

23. Kolokolnikov T, Titcombe MS, Ward MJ. 2005 Optimizing the fundamental Neumann eigenvalue for the Laplacian in a domain with small traps. *Eur. J. Appl. Math.* **16**, 161–200. (doi:10.1017/S0956792505006145)

24. Stepien TL, Zmurchok C, Hengenius JB, Rivera RMC, D'Orsogna MR, Lindsay AE. 2020 Moth mating: modeling female pheromone calling and male navigational strategies to optimize

reproductive success. *Appl. Sci.* **10**, 6543. (doi:10.3390/app10186543)

25. Richards D, Saunders T. 2015 Spatiotemporal analysis of different mechanisms for interpreting morphogen gradients. *Biophys. J.* **108**, 2061–2073. (doi:10.1016/j.bpj.2015.03.015)

26. Meier B, Zielinski A, Weber C, Arcizet D, Youssef S, Franosch T, Rädler JO, Heinrich D. 2011 Chemotactic cell trapping in controlled alternating gradient fields. *Proc. Natl Acad. Sci. USA* **108**, 11 417–11 422. (doi:10.1073/pnas.1014853108)

27. Berg HC, Purcell EM. 1977 Physics of chemoreception. *Biophys. J.* **20**, 193–219. (doi:10.1016/S0006-3495(77)85544-6)

28. Shoup D, Szabo A. 1982 Role of diffusion in ligand binding to macromolecules and cell-bound receptors. *Biophys. J.* **40**, 33–39. (doi:10.1016/S0006-3495(82)84455-X)

29. Bressloff PC, Newby JM. 2013 Stochastic models of intracellular transport. *Rev. Mod. Phys.* **85**, 135–196. (doi:10.1103/RevModPhys.85.135)

30. Northrup SH. 1988 Diffusion-controlled ligand binding to multiple competing cell-bound receptors. *J. Phys. Chem.* **92**, 5847–5850. (doi:10.1021/j100331a060)

31. Handy G, Lawley SD. 2021 Revising Berg-Purcell for finite receptor kinetics. *Biophys. J.* **120**, 2237–2248. (doi:10.1016/j.bpj.2021.03.021)

32. Lawley SD, Miles CE. 2019 How receptor surface diffusion and cell rotation increase association rates. *SIAM J. Appl. Math.* **79**, 1124–1146. (doi:10.1137/18M1217188)

33. Bressloff PC, Karamched BR, Lawley SD, Levien E. 2017 Diffusive transport in the presence of stochastically gated absorption. *Phys. Rev. E* **96**, 022102. (doi:10.1103/PhysRevE.96.022102)

34. Bressloff P, Lawley SD. 2015 Stochastically gated diffusion-limited reactions for a small target in a bounded domain. *Phys. Rev. E* **92**, 062117. (doi:10.1103/PhysRevE.92.062117)

35. Cherry J, Lindsay AE, Navarro Hernández A, Quaife B. 2022 Trapping of planar Brownian motion: full first passage time distributions by kinetic Monte Carlo, asymptotic, and boundary integral methods. *Multiscale Model. Simul.* **20**, 1284–1314. (doi:10.1137/21M146380X)

36. Lawley SD. 2020 Universal formula for extreme first passage statistics of diffusion. *Phys. Rev. E* **101**, 012413. (doi:10.1103/PhysRevE.101.012413)

37. Lawley SD, Madrid JB. 2020 A probabilistic approach to extreme statistics of Brownian escape times in dimensions 1, 2, and 3. *J. Nonlinear Sci.* **30**, 1207–1227. (doi:10.1007/s00332-019-09605-9)

38. Lawley SD. 2020 Distribution of extreme first passage times of diffusion. *J. Math. Biol.* **80**, 2301–2325. (doi:10.1007/s00285-020-01496-9)

39. Ward MJ, Henshaw W, Keller JB. 1993 Summing logarithmic expansions for singularly perturbed eigenvalue problems. *SIAM J. Appl. Math.* **53**, 799–828. (doi:10.1137/0153039)

40. Bressloff PC. 2021 Asymptotic analysis of extended two-dimensional narrow capture problems. *Proc. R. Soc. A* **477**, 20200771. (doi:10.1098/rspa.2020.0771)

41. Bressloff PC. 2022 Accumulation time of diffusion in a two-dimensional singularly perturbed domain. *Proc. R. Soc. A* **478**, 20210847. (doi:10.1098/rspa.2021.0847)

42. Ward MJ, Keller JB. 1993 Strong localized perturbations of eigenvalue problems. *SIAM J. App. Math.* **53**, 770–798. (doi:10.1137/0153038)

43. Lindsay AE, Spoonmore R, Tzou J. 2016 Hybrid asymptotic-numerical approach for estimating first passage time densities of the two-dimensional narrow capture problem. *Phys. Rev. E* **94**, 042418. (doi:10.1103/PhysRevE.94.042418)

44. Weideman JAC. 2006 Optimizing Talbot's contours for the inversion of the Laplace transform. *SIAM J. Numer. Anal.* **44**, 2342–2362. (doi:10.1137/050625837)

45. Abate J, Whitt W. 2006 A unified framework for numerically inverting Laplace transforms. *INFORMS J. Comput.* **18**, 408–421. (doi:10.1287/ijoc.1050.0137)

46. Weideman JAC, Fornberg B. 2022 Fully numerical Laplace transform methods. *Numer. Algorithms* **92**, 985–1006. (doi:10.1007/s11075-022-01368-x)

47. Trefethen LN, Weideman JAC, Schmelzer T. 2006 Talbot quadratures and rational approximations. *BIT Numer. Math.* **46**, 653–670. (doi:10.1007/s10543-006-0077-9)

48. Berezhkovskii AM, Monine MI, Muratov CB, Shvartsman SY. 2006 Homogenization of boundary conditions for surfaces with regular arrays of traps. *J. Chem. Phys.* **124**, 036103. (doi:10.1063/1.2161196)

49. Berezhkovskii AM, Makhnovskii YA, Monine MI, Zitserman VY, Shvartsman SY. 2004 Boundary homogenization for trapping by patchy surfaces. *J. Chem. Phys.* **121**, 11 390–11 394. (doi:10.1063/1.1814351)

50. Bruna M, Chapman SJ, Ramon GZ. 2015 The effective flux through a thin-film composite membrane. *EPL (Europhys. Lett.)* **110**, 40005. (doi:10.1209/0295-5075/110/40005)

51. Lindsay AE, Bernoff AJ, Ward MJ. 2017 First passage statistics for the capture of a Brownian particle by a structured spherical target with multiple surface traps. *Multiscale Model. Simul.* **15**, 74–109. (doi:10.1137/16M1077659)

52. Lindsay AE, Bernoff AJ, Schmidt D. 2018 Boundary homogenization and capture time distributions of semi-permeable membranes with periodic patterns of reactive sites. *Multiscale Model. Simul.* **16**, 1411–1447. (doi:10.1137/17m1162512)

53. Bressloff PC. 2022 The 3D narrow capture problem for traps with semipermeable interfaces. *arXiv.* (doi:10.48550/arXiv.2211.12472)

54. Briggs WL, Henson VE. 1995 *The DFT: an owner's manual for the discrete Fourier transform*. Philadelphia, PA: SIAM.

55. Pillay S, Ward MJ, Peirce A, Kolokolnikov T. 2010 An asymptotic analysis of the mean first passage time for narrow escape problems: part I: two-dimensional domains. *SIAM Multiscale Model. Simul.* **8**, 803–835. (doi:10.1137/090752511)

56. Lindsay AE, Kolokolnikov T, Tzou JC. 2015 Narrow escape problem with a mixed trap and the effect of orientation. *Phys. Rev. E* **91**, 032111. (doi:10.1103/PhysRevE.91.032111)

57. Endres RG, Wingreen NS. 2009 Maximum likelihood and the single receptor. *Phys. Rev. Lett.* **103**, 158101. (doi:10.1103/PhysRevLett.103.158101)

58. Weiner OD, Servant G, Welch MD, Mitchison TJ, Sedat JW, Bourne HR. 1999 Spatial control of actin polymerization during neutrophil chemotaxis. *Nat. Cell Biol.* **1**, 75–81. (doi:10.1038/10042)

59. Allen C, Broom M, Chadwick V. 1992 Flow cytometry analysis of the expression of neutrophil FMLP receptors. *J. Immunol. Methods* **149**, 159–164. (doi:10.1016/0022-1759(92)90246-P)

60. Whorton MR, Bokoch MP, Rasmussen SGF, Huang B, Zare RN, Kobilka B, Sunahara RK. 2007 A monomeric G protein-coupled receptor isolated in a high-density lipoprotein particle efficiently activates its G protein. *Proc. Natl Acad. Sci. USA* **104**, 7682–7687. (doi:10.1073/pnas.0611448104)

61. Chandrasekaran A, Ellett F, Jorgensen J, Irimia D. 2017 Temporal gradients limit the accumulation of neutrophils toward sources of chemoattractant. *Microsyst. Nanoeng.* **3**, 16067. (doi:10.1038/micronano.2016.67)

62. Trefethen LN. 2018 Series solution of Laplace problems. *ANZIAM J.* **60**, 1–26. (doi:10.1017/S1446181118000093)

63. Iyaniwura S, Ward MJ. 2021 Asymptotic analysis for the mean first passage time in finite or spatially periodic 2D domains with a cluster of small traps. *ANZIAM J.* **63**, 1–22. (doi:10.21914/anziamj.v63.15976)